Jefferson Lab PAC 30 Proposal

Measurement of the Charged Pion Form Factor to High Q^2

July 7, 2006

G.M. Huber (Co-spokesperson), G.J. Lolos, Z. Papandreou
University of Regina, Regina, SK, Canada

P. Bosted, A. Bruell, R. Ent, H.C. Fenker, D. Gaskell (Co-spokesperson), T. Horn, M.K. Jones, D. Mack, D. Meekins, G.R. Smith, S.A. Wood
Physics Division, TJNAF, Newport News, VA

A. Asaturyan, A. Mkrtchyan, H. Mkrtchyan, T. Navasardyan, V. Tadevosyan
Yerevan Physics Institute, Yerevan, Armenia

D. Dutta, H. Gao, X. Qian, X.F. Zhu
Duke University, Durham, NC

W. Boeglin, P. Markowitz, J. Reinhold
Florida International University, Miami, FL

E. Christy, C.E. Keppel, V. Tvaskis
Hampton University, Hampton, Virginia

E. Beise, H. Breuer
University of Maryland, College Park, MD

R. Gilman, J. Roche
Rutgers University, Piscataway, NJ

W. Kim, S.S. Stepanyan
Kyungpook National University, Daegu, Republic of Korea

E.J. Brash
Christopher Newport University, Newport News, VA

E. Gibson
California State University, Sacramento, CA

D. Hornidge
Mount Allison University, Sackville, NB, Canada

P.M. King
University of Illinois, Urbana-Champaign, IL

E. Korkmaz
University of Northern British Columbia, Prince George, BC, Canada

A.K. Opper

The George Washington University, Washington, DC

I. Niculescu

James Madison University, Harrisonburg, VA

C.F. Perdrisat

College of William and Mary, Williamsburg, VA

A. Sarty

Saint Mary's University, Halifax, NS, Canada

C. Xu

Institute of Particle Physics, Central China Normal University, Wuhan, P.R. China

I. CONTRIBUTION TO THE HALL C 12 GEV UPGRADE

The co-spokespersons for this experiment plan to contribute to the implementation of the Hall C upgrade for 12 GeV in both manpower and materials.

Garth Huber intends to apply to the Natural Sciences and Engineering Research Council of Canada (NSERC) for a Research Tools and Instrumentation grant (approximately $100kUSD) in support of the SHMS Heavy Gas Čerenkov detector. Given the currently-projected CD2 and CD3 review schedule, this application will likely be submitted in October, 2008. Should these funds be granted by the Government of Canada, he intends to lead the construction efforts of this detector in collaboration with Hall C scientific and technical staff. In either event, the Regina group intends to provide manpower in support of the R&D, construction and commissioning of this detector.

David Gaskell will support the SHMS construction and detector assembly as part of his general Hall C support duties. In addition, he will devote a significant fraction of his "Research" time to work on the Hall C upgrade. In particular, he will devote time to updating and maintaining the Hall C simulation package SIMC. This will entail, not only incorporating the SHMS into the existing simulation, but helping with spectrometer optics calculations to guide the design and construction of the SHMS.

II. SUMMARY

At JLab, we have a unique opportunity to dramatically improve the F_π database. Much can be learned about the usefulness of QCD sum rules and relativistic potential models for understanding the structure of the pion in the (presumably) difficult and non-perturbative Q^2 regime of 1-6 GeV^2.

This proposal deals with the continuation of our successful Hall C F_π program. Using the HMS+SOS spectrometers in Hall C and beam with energy up to 5.25 GeV, we have recently obtained data for the charged pion form factor (F_π) up to Q^2=2.45 GeV^2. We now propose to continue these measurements to dramatically higher Q^2, to test QCD-based models of hadron structure in the most rigorous manner. This requires the separation of the L/T/LT/TT terms in exclusive $p(e,e'\pi^+)n$ data at low $-t < 0.2$ GeV^2, W well above the resonance region ~ 3 GeV, and over a wide range of Q^2. We also propose a measurement at Q^2=0.30 GeV^2, near the upper limit of the F_π values determined exactly from π^+ elastic scattering data, as a definitive test of the electroproduction method of extracting F_π. These data will allow the charged pion form factor to be extracted with unprecedented accuracy and precision, and provide a meaningful test of QCD-based models in the transition region between perturbative and non-perturbative QCD.

The data to be acquired falls into the following categories:

1. $p(e,e'\pi^+)n$ L/T separated data for Q^2 = 1.6-6.0 GeV^2 and W near 3 GeV. The data at Q^2=1.60 and 2.45 GeV^2 will be 70% closer to the pion pole than our earlier E93-021 (Fpi-1) and E01-004 (Fpi-2) data taken at much lower W, and so will be an excellent probe of the model-dependence of the extracted F_π result in this Q^2 range. The Q^2 = 3.50-6.00 GeV^2 data will probe the onset of pQCD in a simple quark system. These data will be of dramatically higher quality than the existing Cornell data in this region.

2. Low Q^2 = 0.30 GeV^2 data taken extremely close to the pion pole, $-t_{min}$ = 0.005 GeV^2, to cross check the extracted F_π values using the electroproduction method against those obtained without approximation from elastic π^+e^- scattering at the CERN SPS. Our data will have 50% smaller $-t$ than any previous electroproduction data, and hence be a sensitive test of the electroproduction method.

3. Exclusive π^-/π^+ ratio measurements using a liquid deuterium target at selected Q^2, as a test of the t-channel dominance of the $d\sigma_L$ data.

4. Extensive elastic scattering measurements to calibrate the spectrometer detectors and acceptances, and to measure kinematic offsets. Elastic ep scattering is proposed to be used in both singles and coincidence modes. Additional (inelastic) data from thin carbon targets will be taken for spectrometer pointing studies and optics checks.

III. SCIENTIFIC MOTIVATION

The π^+ electric form factor is a topic of fundamental importance to our understanding of hadronic structure. It is well known [1] that the asymptotic behavior is rigorously calculable in perturbative QCD (pQCD), with value

$$F_\pi(Q^2 \to \infty) \to \frac{8\pi\alpha_s f_\pi^2}{Q^2},$$

where $f_\pi = 133$ MeV is the $\pi^+ \to \mu^+\nu$ decay constant. This result is in principle exact, and is dependent only on the assumption of quark asymptotic freedom.

The theoretical prediction for F_π at experimentally accessible Q^2 is less certain, as soft contributions, such as gluonic effects, must be explicitly taken into account. This is a difficult and poorly understood region, but there has been considerable progress in our understanding around which value of Q^2 the hard scattering (asymptotic QCD) part of the pion form factor will dominate. Unfortunately, it is generally expected that the asymptotic region is well beyond the capabilities of Jefferson Lab, even after the energy upgrade, probably near $Q^2 = 20$ GeV^2 (e.g.[2–7]).

The most interesting question then, as far as Jefferson Laboratory is able to address, is the description of $F_\pi(Q^2)$ in the gap between the "soft" and "hard" regions. For example, Jakob and Kroll [4] found that a self consistent treatment of the pQCD contribution to the pion form factor in the few GeV region requires the inclusion of both Sudakov corrections and the transverse momenta of the quarks, leading to an amount which is nonetheless too small with respect to the data, and leaving room for an important role of other processes, such as higher twists. These calculations were subsequently extended to next-to-leading order [8, 9], but the conclusions are similar. Taking a different approach, Braun, Khodjamirian, and Maul [10] performed a light-cone sum rule calculation up to twist 6, and found that the non-perturbative hard contributions of higher twist strongly cancel the soft components, even at relatively modest Q^2. It is clear from these works that special attention must be applied theoretically to the interplay of soft and hard contributions at intermediate momentum transfer. Reliable experimental data are a necessary component in these studies to delineate the role of hard versus soft contributions at intermediate Q^2, and so guide these theoretical investigations.

On the 'soft' front, the pion form factor is also an important observable because it can be calculated in a wide variety of theoretical approaches. In this sense, F_π plays a role similar to that of the positronium atom in QED. Hwang [11] used a relativistic quark model on the light front, which allows a consistent and fully relativistic treatment of quark spins and center-of-mass motion to be carried out. The wave function parameters are determined from experimental data on the charged pion decay constant, the neutral pion two-photon decay width, and the charged pion electromagnetic radius, and then the charge and transition

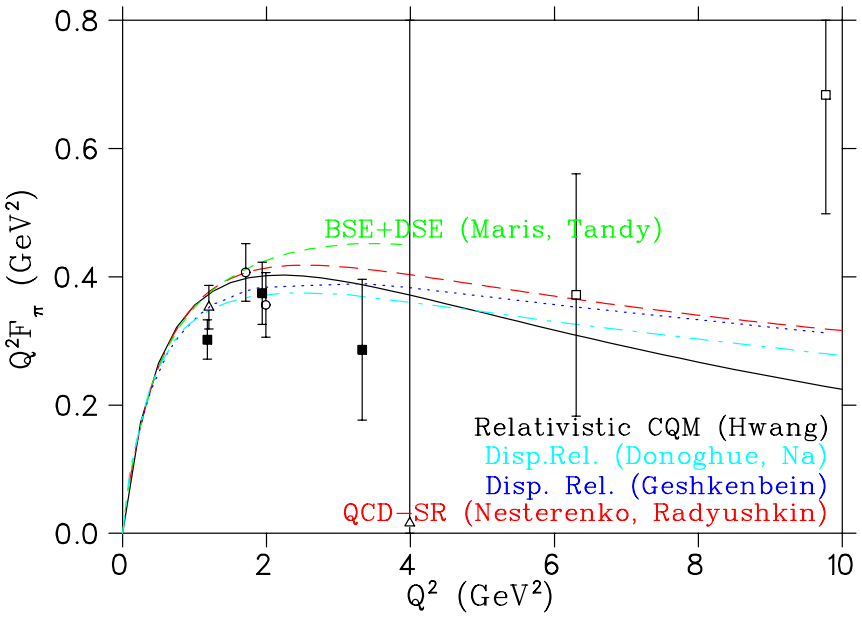

FIG. 1: Predictions of five selected F_π models at intermediate Q^2. There are of course dozens of calculations to choose from, these represent the range of variation in our present theoretical knowledge. With the exception of the QCD sum-rule calculation of Ref. [13], all of the other calculations are constrained by various experimental data. The data points are the Cornell data listed in Table II; only the solid points correspond to L/T separations.

form factors of the pion and neutral pion are predicted. Maris and Tandy [12] use the Bethe-Salpeter plus Dyson-Schwinger equations with a momentum dependent dressing of the quarks to determine the pion form factor. The model's parameters are adjusted to reproduce m_π, f_π, and $\langle\bar{q}q\rangle$, then predicted the pion radius and F_π. Nesterenko and Radyushkin [13] use the QCD sum-rule approach in combination with a hard model based on the Ward identity to predict $F_\pi(Q^2)$ with no free parameters. Finally, Geshkenbein [14] uses the dispersion relation technique with added QCD constraints to relate F_π in the timelike and spacelike regions. All of these approaches yield essentially identical F_π predictions consistent with the measured π^+ charge radius at low Q^2, and then progressively diverge (Fig. 1). Extending the range with reliable experimental data to values of Q^2 beyond where they exist now is clearly needed.

The difficult intermediate Q^2 regime is a vital one where one can gauge the success of a variety of calculations of hadron structure, and the pion is the first test case that all must consider as the situation for the nucleonic form factors is even more complicated. Firstly, their asymptotic behavior is not predicted in such an unequivocal manner. Secondly, the greater number of valence quarks in the nucleon means that the asymptotic regime will be reached at much higher values of Q^2, at least 100 GeV^2[2]. Finally, the lower power of Q^2 in

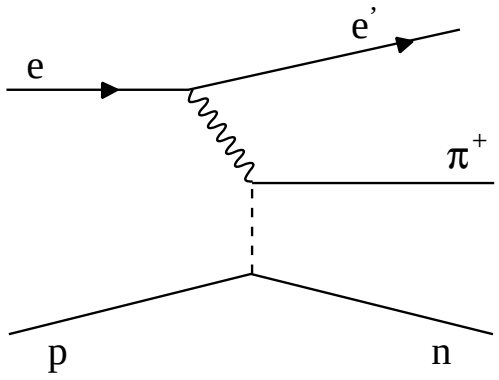

FIG. 2: Diagram of the t-channel process.

the pion form factor means that the relevant cross section will be more easily accessible, and less sensitive to experimental uncertainties in Q^2. Because of these reasons, if one believes that it is worthwhile to pursue the measurement of a hadronic form factor where perturbative effects may become apparent, the pion form factor is the obvious first choice.

IV. HOW TO DETERMINE F_π

Due to the extensive experience gained during ongoing F_π measurements in Hall C, as well as lessons learned from previous work at Cornell and DESY, many of the experimental difficulties in extracting the pion form factor are well understood. There are a number of issues of importance:

1. To perform measurements above $Q^2 = 0.3$ GeV^2, one must employ electron scattering off the virtual π^+ (associated with the "pion cloud" of the proton), and relate the resulting measurement to the on-shell electron-pion scattering amplitude. The dependence on F_π enters the cross section via the t-channel diagram (Fig. 2), which in Born term models [15] is given as

$$\frac{d\sigma_L}{dt} \sim \frac{-tQ^2}{(t-m_\pi^2)^2} g_{\pi NN}^2(t) F_\pi^2(Q^2).$$

   The virtual nature of the pion target comes is apparent via the term $g_{\pi NN}(t)$, which can be seen as the probability amplitude to have a virtual π^+ inside the proton at a given t. An additional complication is that the physical region for t in pion electroproduction is negative, while real electron-pion scattering corresponds to $t = m_\pi^2$.

   For W above the resonance region, the t-channel diagram dominates σ_L for small $|t|$ and contributes unequally to the L, T, TT, and LT responses. The competing non-pole production diagrams contribute to σ_L as well, but they are small in forward

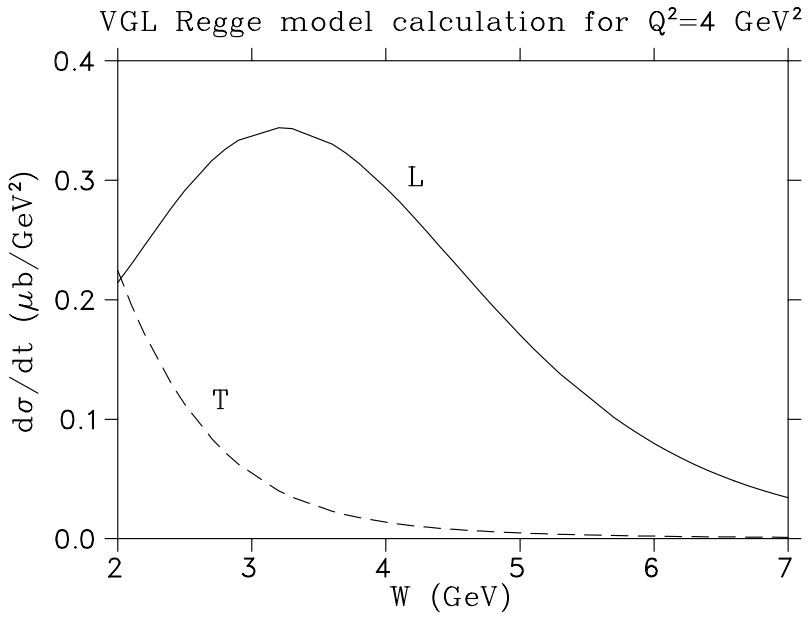

FIG. 3: VGL Regge model [16] calculation of the L and T terms in the $p(e,e'\pi^+)n$ reaction at $Q^2 = 4$ GeV^2, at t_{min}. The model parameters are $\Lambda_\pi^2 = 0.462$ GeV^2, $\Lambda_\rho^2 = 1.5$ GeV^2. Note that the VGL model tends to underestimate $\sigma_{\rm T}$, as is discussed later in Fig. 16.

kinematics (i.e. small $|t|$) and do not have a pole at $t = m_\pi^2$. Therefore, to maximize the contribution of the t-channel diagram, as well as separate it from the others which tend to disguise its effect, it is absolutely necessary to measure at a low $|t|$ in parallel and near-parallel kinematics, and to perform a response function separation.

The 12 GeV upgrade is essential for these measurements, because it allows a higher W to be accessed, which results in data obtained at a dramatically lower $|t|$ than previously possible. Regge model [16] calculations indicate that there is in fact a range of W for which the contribution of the t-channel diagram is optimized (Fig. 3). $-t_{min}$ decreases (i.e. gets closer to the π^+ pole) from left to right on the figure, with value $t = -0.53$ at $W = 2$, $t = -0.14$ at $W = 3$, and $t = -0.05$ at $W = 4$ GeV. Nonetheless, $d\sigma_L/dt$ drops dramatically above $W = 3.5$ GeV, and so the optimal value of W for a measurement at $Q^2 = 4$ GeV^{2}is near $W = 3.2$ GeV.

The kinematics we propose for this measurement are consistent with these requirements.

2. The presence of isoscalar backgrounds to σ_L can be inferred by measuring the ratio

$$P = \frac{\sigma(n(e,e'\pi^-)p)}{\sigma(p(e,e'\pi^+)n))} = \frac{|A_v - A_s|^2}{|A_v + A_s|^2}.$$

The t-channel diagram is a purely isovector process, and so at small $|t|$, P should be

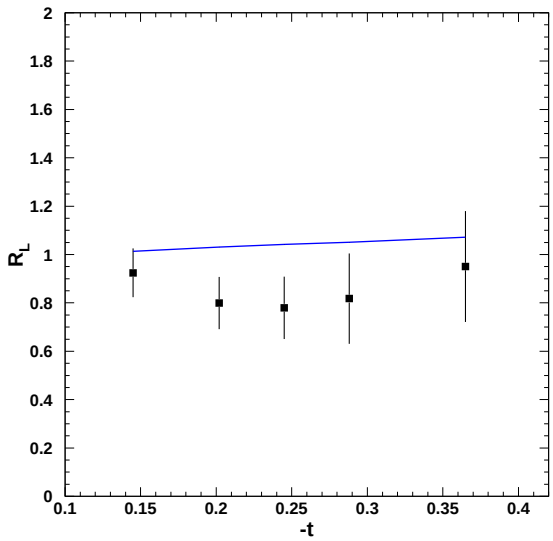

FIG. 4: Preliminary π^-/π^+ ratios for $\sigma_{\rm L}$ at Q^2=2.45 GeV^2 from the Fpi-2 experiment. The curve near unity indicates the VGL Regge model prediction with $\Lambda_\pi^2 = 0.491$ GeV^2 and $\Lambda_\rho^2 = 1.7$ GeV^2. Note that the systematic errors (not shown) on this ratio are still rather large at this stage of the analysis (5-10%)

near unity. Isoscalar backgrounds are expected to be suppressed by the L response function extraction. Nonetheless, if they are present to any significant degree, they will result in a dilution of the ratio. These tests were performed in E01-004 (Fpi-2), and a preliminary σ_L ratio consistent with unity, as well as with VGL Regge model expectations, was obtained (Fig. 4).

The tests performed during the Fpi-1 and Fpi-2 experiments give us confidence that at low $-t$ isoscalar backgrounds are not a significant issue for the extraction of F_π. Here, we propose to explore a new kinematic regime, $W \approx 3$ GeV, where we hope the situation to be even more favorable. Nonetheless, we believe it will be prudent to perform a few more checks at this larger W, although we limit the tests to kinematic settings where the beam time impact is not large.

The bottom line is that tests can and must be performed to verify that the longitudinal data are dominated by the t-channel process. This lends confidence in the F_π value extracted from the experiment.

3. It is absolutely essential to use theoretical input for the extraction of F_π.

   Frazer [17] originally proposed that F_π be extracted from σ_L via a kinematic extrapolation to the pion pole, and that this be done in an analytical manner, à la Chew-Low.

The Born formula, given earlier, is not gauge invariant [16], but should nonetheless give F_π, in principle, when extrapolating to the pole. However, this extrapolation procedure fails to produce a reliable answer, since different polynomial fits, each of which are equally likely in the physical region, differ considerably when continued to $t = m_\pi^2$. Some attempts were made [18] to reduce this uncertainty by providing some theoretical constraints on the behavior of the pion form factor in the unphysical region, but none proved adequate.

Bebek et al. [19] embraced the use of theoretical input when they used the Born term model of Berends [15] to perform a form factor determination. Brauel et al. [20] similarly used the Born term model of Gutbrod and Kramer [21] to extract F_π. The presence of the nucleon and its structure complicates the theoretical model used, and so an unavoidable implication of this method is that the extraction of the pion form factor becomes model dependent.

Similarly, Jefferson Lab E93-021 (Fpi-1) [22, 23] and E01-004 (Fpi-2) [24] used the Regge model of Vanderhaeghen, Guidal, and Laget [16] to extract F_π. In this model, the pole-like propagators of Born term models are replaced with Regge propagators, and so the interaction is effectively described by the exchange of a family of particles with the same quantum numbers instead of the exchange of one particle. The model incorporates both the π ($J = 0$) and the ρ ($J = 1$) trajectories, with free parameters $\Lambda_{\pi,\rho}$, the π, ρ trajectory cutoff parameters, and fully takes into account off-shell effects without requiring a $g_{\pi NN}(t)$ factor. The Regge model does a superior job of describing the t dependence of the differential pion electroproduction cross sections of [20, 25] than the Born term model. Since the Regge model assumes a monopole form factor

$$F_\pi(Q^2) = [1 + Q^2/\Lambda_\pi^2]^{-1}, \tag{1}$$

Λ_π is varied to obtain the best fit with the σ_L data, and F_π for that Q^2 found from substitution of Λ_π into the above equation.

Obukhovsky, et al., [26] are developing a quark model description of the $p(e, e'\pi^+)n$ reaction which might also be appropriate for extraction of the pion form factor. Before it can be reliably applied to our data, there are some remaining theoretical issues which the authors need to resolve. In principle, the experimentalist would like to use a variety of models to extract F_π from the electroproduction data, so that the model dependence of the extraction of the form factor can be better understood. It is also important to point out that because our experimentally measured $d\sigma_L/dt$ will be published in the literature, updated values of F_π could be extracted in the future, should even more sophisticated models for the $p(e, e'\pi^+)n$ reaction become available. The experimental result is not permanently 'locked in' to a specific model.

A. JLab data and analysis

As an example of what is feasible at JLab, we present some results from the recently completed E01-004 (Fpi-2) experiment [24]. This experiment measured F_π with the HMS+SOS spectrometers in Hall C.

The cross section for pion electroproduction can be written as

$$\frac{d^3\sigma}{dE' d\Omega_{e'} d\Omega_\pi} = \Gamma_V J(dtd\phi \rightarrow d\Omega_\pi)\frac{d^2\sigma}{dtd\phi}, \tag{2}$$

where Γ_V is the virtual photon flux factor, J is the Jacobian that transforms the virtual photon cross section from t, ϕ to the pion solid angle, ϕ is the azimuthal angle of the outgoing pion with respect to the electron scattering plane and t is the Mandelstam variable $t = (p_\pi - q)^2$. The two-fold differential cross section can be written as

$$\begin{aligned} 2\pi\frac{d^2\sigma}{dtd\phi} \;=\; & \epsilon\frac{d\sigma_{\rm L}}{dt} + \frac{d\sigma_{\rm T}}{dt} + \sqrt{2\epsilon(\epsilon+1)}\,\frac{d\sigma_{\rm LT}}{dt}\cos\phi \\ & + \epsilon\frac{d\sigma_{\rm TT}}{dt}\cos 2\phi. \end{aligned} \tag{3}$$

The cross sections $\sigma_X \equiv \frac{d\sigma_{\rm X}}{dt}$ depend on W, Q^2, and t. The longitudinal cross section $\sigma_{\rm L}$ at small $-t$ is dominated by the t-pole term, which contains F_π. The ϕ acceptance of the experiment allows the combination $\epsilon\sigma_{\rm L}+\sigma_{\rm T}$, and the interference terms $\sigma_{\rm LT}$ and $\sigma_{\rm TT}$ to be determined. Data at least two energies are required at every Q^2, so that $\sigma_{\rm L}$ can be separated from $\sigma_{\rm T}$ by means of a Rosenbluth separation. The kinematics used in the two JLab experiments are listed Table I.

In parallel kinematics, it is not possible to hold W and Q^2 fixed, and still vary $-t$, since in this case they are not independent variables. In order to measure the dependence of σ_L versus t, to test the success of the Regge model and aid in the extraction of F_π, θ_π was varied away from parallel kinematics. In this case, the LT and TT terms also contribute, and so additional data at $\pm 3^o$ from parallel kinematics were obtained to complete the ϕ-coverage at the high ϵ setting (where the pion arm was at sufficiently large angle to allow this). These response functions were obtained from the ϕ dependence of the data, and incorporated in the extraction of σ_L (Fig. 5).

Fig. 6 shows the L and T separated cross sections from E01-004, plotted versus $-t$. This dependence on $-t$ was obtained by making full use of the acceptance of the spectrometers. It is seen in Fig. 6 that that the Regge model predictions are in good agreement with the σ_L data, but do not agree well with the σ_T data. However, since σ_L is dominated at small $|t|$ by the t-channel process, other processes should have only limited influence on the extraction of F_π from σ_L. This was checked by varying the ρ trajectory cutoff parameter, Λ_ρ. While this caused a large change in the prediction for σ_T, σ_L was nearly unaffected. The F_π values at the two Q^2 were obtained from the best fit values of Λ_π and equation 1.

TABLE I: Central arm kinematics used in E93-021 (Fpi-1) and E01-004 (Fpi-2). Note that at their common Q^2=1.60 GeV^2 point, W is higher in Fpi-2, leading to a smaller value of $-t$ and corresponding smaller model uncertainties in the extraction of F_π from the data.

Q^2	W	E_e	$\theta_{e'}$	$E_{e'}$	θ_q	p_π	ϵ	$\lvert t\rvert$
(GeV^2)	(GeV)	(GeV)	(deg)	(GeV)	(deg)	(GeV/c)		(GeV^2)
E93-021 (Fpi-1) Kinematics								
0.60	1.95	2.445	38.40	0.567	9.99	1.856	0.375	0.030
		3.548	18.31	1.670	14.97	1.856	0.737	0.030
0.75	1.95	2.673	36.50	0.715	11.46	1.929	0.430	0.044
		3.548	21.01	1.590	15.45	1.929	0.704	0.044
1.00	1.95	2.673	47.26	0.582	10.63	2.048	0.327	0.071
		3.548	25.41	1.457	15.65	2.048	0.647	0.071
1.60	1.95	3.005	56.49	0.594	10.49	2.326	0.272	0.150
		4.045	28.48	1.634	16.63	2.326	0.626	0.150
E01-004 (Fpi-2) Kinematics								
1.60	2.21	3.772	43.08	0.786	9.53	2.931	0.328	0.095
		4.701	25.72	1.716	13.28	2.931	0.593	0.095
2.45	2.21	4.210	51.48	0.771	9.19	3.336	0.270	0.186
		5.248	29.43	1.809	13.61	3.336	0.554	0.186

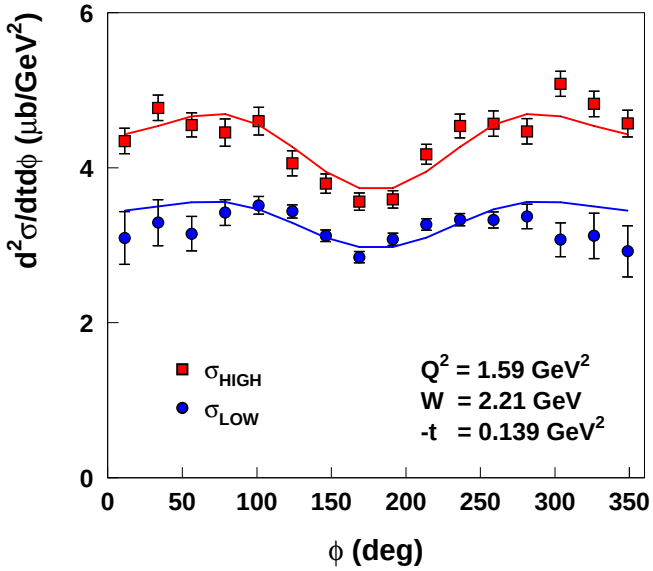

FIG. 5: Unseparated cross sections at high and low ϵ from E01-004. The data ϕ distributions are used to determine the LT and TT response functions, while the ϵ dependence gives σ_L. The curves represent the model cross section used in the Monte Carlo simulation.

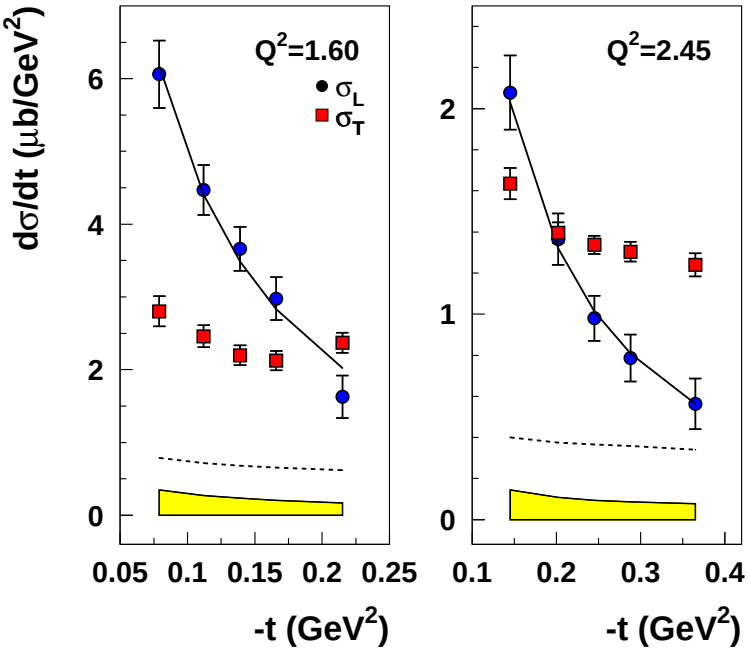

FIG. 6: Separated cross sections $\sigma_{\rm L}$ and $\sigma_{\rm T}$ from E01-004 compared to the VGL Regge model (full curve for L, dashed curve for T) with parameters $\Lambda_\pi^2 = 0.513(0.491)$ GeV^2 and $\Lambda_\rho^2 = 1.1$ GeV^2. Because of the various kinematic correlations, each t-bin has its own average $\overline{W}$ and $\overline{Q^2}$ which differ slightly from the nominal values. The error bars indicate the statistical and uncorrelated systematic uncertainty in both ϵ and t combined in quadrature; the error band denotes the correlated part of the systematic uncertainty by which all data points move collectively.

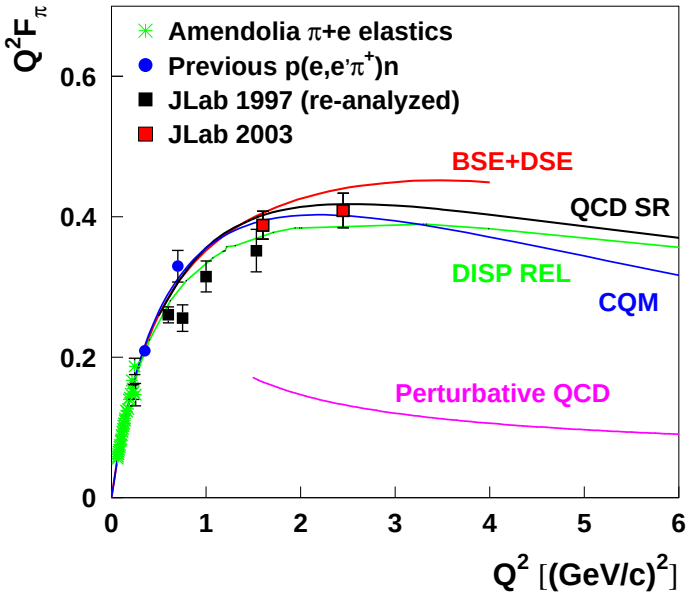

FIG. 7: F_π data from E01-004 compared with precision results from older experiments and theoretical calculations, as noted.

Fig. 7 shows our F_π results from E93-021 and E01-004. While the E01-004 measurements have significantly smaller errors than the E93-021 measurements, the two sets are consistent with each other at their common Q^2=1.6 GeV^2 point. The Fpi-2 data are taken at higher W and hence smaller $-t$ than the Fpi-1 data (see Table I) and so it is expected to be the more reliable of the two. The good agreement between these two measurements, with different experimental and model systematic uncertainties, lends confidence that this experimental method can be applied with success at even higher Q^2.

B. Interpretability issues with the older high Q^2 data and analyses

Unfortunately, the experimental knowledge of F_π above $Q^2 = 2.45$ GeV^2 is poor. Until 1978, the pion form factor in the space-like region was an active and mature field, after which time it went into dormancy due to the limitations of the available electron accelerators. The perception that F_π is difficult or impossible to extract at high Q^2 stems from the poor quality of these old data. Table II summarizes the conditions under which they were obtained.

Table II shows that the situation above $Q^2 = 2.0$ GeV^2 degrades rapidly. For example, Bebek et al. [19] were unable to perform a L/T separation, and so were sensitive to the presence of isoscalar backgrounds. They were required to add an empirical isoscalar component to the theory of Berends before performing a F_π extraction, amounting to an approximately 10% correction. Where they were able to perform a L/T separation, the resulting uncertainties in σ_L were so large that for the actual determination of the pion form factor, σ_T was simply assumed to be proportional to the total photon cross section and subtracted from the measured (differential) cross section to arrive at σ_L. Since no uncertainty was used in the assumed values of σ_T, the given uncertainties in their extracted values for F_π are (severely) underestimated. This, together with the already relatively large statistical and systematic uncertainties of those data, precludes a meaningful comparison with theoretical calculations, and led Carlson and Milana to conclude *"[we] question whether F_π has been truly determined for large Q^2"* [30].

In Ref. [30], Carlson and Milana point out that the existence of competing non-pole QCD processes complicate the extraction of F_π at large Q^2. This criticism stems from the large size of $|t|$ used in the Table II results, several of which have $-t_{min} > 20m_\pi^2$. The backgrounds calculated for a number of the above results are reproduced in Table III. It is seen that the background ratio M_{pQCD}/M_{pole} rises dramatically once $-t_{min} > 0.20$. In order to avoid this problem *"more reliable measurements of F_π at high Q^2 require smaller $|t|$ and thus higher electron energy loss ν."*[30].

The issue of non-pole backgrounds was revisited by Mankiewicz, Piller and Radyushkin [31] by formulating pseudoscalar and pseudovector pion production mechanisms in terms of the quark double distribution functions of the nucleon; i.e. the existence of the pion-pole

TABLE II: Description of old DESY and Cornell data. Pay particular attention to the large values of $|t|$ used for the large Q^2 measurements, and the poor attention to systematic errors. These Cornell data are displayed in Fig. 1.

Q^2 (GeV^2)	W (GeV)	$-t_{min}$ (GeV^2)	Reference	Comments
0.70	2.19	0.05	[20]	Full L/T separation and controlled systematics.
1.20	3.08	0.019	[27]	High ϵ unseparated cross sections only. Hydrogen and π^-/π^+ data on deuterium data taken, and used for isoscalar correction to unseparated cross sections.
3.99	2.14	0.477	[27]	Same.
1.71	3.09	0.034	[27]	High ϵ unseparated cross sections only. Only hydrogen data taken. Isoscalar correction taken from π^-/π^+ measurements on deuterium at other kinematics.
1.99	2.14	0.157	[27]	Same.
1.18	2.11	0.069	[28]	High and low ϵ measurements obtained in different experiments, and combined for L/T separation later. Systematic error?
1.94	2.67	0.07	[28]	Same.
3.33	2.63	0.162	[28]	Same.
6.30	2.66	0.43	[29]	Only low ϵ data taken and t-channel Born Term model used to extract F_π. Uncontrolled systematic errors!
9.77	2.63	0.87	[29]	Same.

contribution fits into the pQCD factorization framework. At the $Q^2 = 10$ GeV^2 they computed, the optimal region governed by the pseudoscalar pion-cloud contribution was found to be $0.2 < x_{Bj} < 0.4$, while at much lower x_{Bj} "the relation to the pion electromagnetic form factor seems to be lost." The lower x_{Bj} limit sets a maximum value to W which is far above those accessible at JLab, while their optimum x_{Bj} region is consistent with the optimal t region found by Carlson and Milana.

Given the success of E01-004, and the estimate of the non-pole background by Carlson and Milana [30], we are fully confident that we will be able to reliably extract F_π for $-t_{min}$ up to 0.20 in this proposed experiment.

TABLE III: The ratio M_{pQCD}/M_{pole} from Ref. [30], using the King-Sachrajda nucleon distribution amplitude, as calculated for a number of high Q^2 results in Table II.

Q^2 (GeV^2)	W (GeV)	$-t$ (GeV^2)	M_{pQCD}/M_{pole}
		0.01	0.18
1.94	2.67	0.07	0.12
3.33	2.63	0.17	0.18
6.30	2.66	0.43	0.81
9.77	2.63	0.87	2.82

V. PROPOSED KINEMATICS

Q^2 =0.30 GeV^2:

A key component of this experiment is to provide precision data with which we can further test the method by which we extract F_π, i.e. the use of the virtual pion cloud of the proton. To that end, we plan to make a measurement at $Q^2 = 0.3$ GeV^2 to perform a direct comparison with exact F_π values measured in $e-\pi$ elastic scattering as a sensitive test of the electroproduction method of determining F_π.

The most recent elastic scattering data were obtained with the scattering of 300 GeV pions from the CERN SPS from atomic electrons [32]. Because of the unfavorable momentum transfer, these data are restricted to the range $Q^2 < 0.253$ GeV^2. F_π values obtained in this manner are exact and have no uncertainty due to model dependence. The electroproduction data which are closest to this limit were obtained at Q^2=0.35 GeV^2 at DESY [25]. The extrapolation of this result to the limit of the elastic scattering data using the monopole parameterization of the form factor shows that they are consistent within uncertainties.

The JLab upgrade will allow us to perform a sensitive test of the electroproduction method with only a modest investment of beam time. We propose to acquire data at Q^2=0.30 GeV^2 with $-t_{min} = 0.005$ GeV^2, which is a 50% smaller $-t$ than any previous electroproduction data.

Q^2 =1.60 and 2.45 GeV^2:

We plan to repeat the $Q^2 = 1.6$ and 2.45 GeV^2 measurements taken in the first and second phases of the F_π program, but at higher $W \approx 3$ GeV and hence much smaller $-t_{min}$. The three sets of measurements (Fpi-1, Fpi-2, and this proposal) at common Q^2 but widely different W and t_{min}, will help us to much better understand the model-dependence of our F_π results. In both the Fpi-1 and Fpi-2 analyses, while the VGL Regge model provides an

acceptable description of $\sigma_{\rm L}$, it has consistently underestimated $\sigma_{\rm T}$ by a large factor. The model dependence of the F_π extraction is expected to be reduced if the measurements are performed at higher W, as proposed here.

Furthermore, the coincidence rates afforded at Q^2=2.45 GeV^2 allow us to efficiently perform measurements at four different ϵ, to provide more comfort/proof that the linearity and thus the SHMS+HMS acceptance knowledge is sound.

Q^2 =3.50, 4.50, 5.25 and 6.0 GeV^2:
One of the primary goals of this proposed measurement is to extend our knowledge of the charged pion form factor to the largest possible Q^2. Given the constraints imposed by the requirement to keep $-t_{min} \leq 0.2$, combined with the maximum beam energy of the upgraded CEBAF and kinematic reach of the SHMS+HMS combination in Hall C, the maximum Q^2 is near 6 GeV^2. At this point, the precision of the measurement may begin to suffer because $-t_{min}$ takes the maximum value indicated by Ref. [30] and because $\Delta\epsilon$ is kinematically restricted. Therefore, we also choose to make a measurement "nearby" at $Q^2 = 5.25$ GeV^2, where the final precision is expected to be better. The points at $Q^2 = 3.5$ GeV^2 and $Q^2 = 4.5$ GeV^2 will be crucial if the highest Q^2 points suggest a "turnover" and that F_π may be beginning to approach the limit of perturbative QCD. Furthermore, these data are acquired relatively quickly and so do not contribute greatly to the total beam time request.

We will make coincidence measurements between charged pions in the SHMS and electrons in the HMS. Since the SHMS will detect pions close to the direction of $\vec{q}$, the dominant contribution will be due to the pion pole diagram. Only events with $\theta_{\pi q}$ near zero degrees are useful, so a high luminosity spectrometer system like the SHMS+HMS is well suited to the measurement. To determine $\sigma_{\rm L}$ from the cross section data, a minimum of two beam energies are needed for each Q^2. Here, however, we propose to take data with three beam energies for each Q^2, with the exception of Q^2=2.45 GeV^2, where we will take four. While the middle ϵ setting will not necessarily reduce the final statistical on the extraction of F_π, it allows a degree of redundancy crucial for the clean determination of systematic uncertainties. We have also been mindful to keep the number of linac gradient settings to a minimum, and to use the 'standard 12 GeV gradient' of 2.15 GeV/pass wherever possible.

Table IV shows the 'near parallel' kinematics settings proposed for the experiment. When selecting our kinematics for this experiment, we have assumed that the SHMS can be set to angles ranging from 5.5^o to 30.0^o, the HMS to angles no smaller than 10.5^o, and that the minimum opening angle between the two spectrometers can be no less than 18.0^o. At each Q^2, we plan to acquire data for three ϵ settings, spanning $\Delta\epsilon \sim 0.3$, and 0.4 where possible. This is feasible for all but our highest Q^2 data, where $\Delta\epsilon \sim 0.26$ is the best

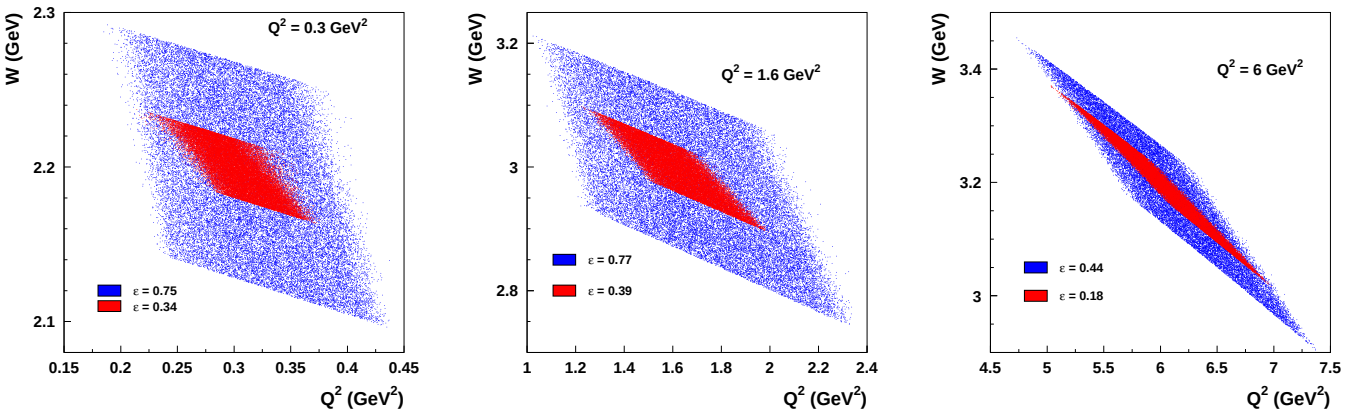

FIG. 8: Simulated Q^2 versus W coverage for the SHMS+HMS combination at Q^2=0.3, 1.60, and 6.0 GeV^2. The red points are the lowest ϵ setting, and the blue points are the highest ϵ setting. The middle ϵ setting is not shown.

that can be achieved. These measurements can be accomplished using three special linac gradients of 1.96 GeV/pass, 1.82 GeV/pass, and 1.37 GeV/pass, in addition to the standard 12 GeV tune. These are indicated in the left-most column of Table IV, where the letter in parentheses indicates the linac gradient and the number preceding it indicates the pass number.

Figure 8 shows the range of Q^2 and W accepted by the spectrometers at three different values of Q^2. Cuts will be placed on the data to equalize the Q^2-W range measured by the three ϵ settings. The Fpi-2 experiment acceptance was similar to the tilted diamond in the rightmost panel of Fig. 8, but the more-square acceptance at low Q^2 in the center and left panels is highly desirable, as it will allow the Q^2 and W dependences of the cross section to be more easily disentangled.

As stated earlier, it is necessary to measure the reaction's $-t$ dependence in order to extract F_π from the $\sigma_{\rm L}$ data. Unfortunately, it is not possible to hold W and Q^2 fixed in parallel kinematics, and still vary $-t$. Therefore, it is necessary to obtain data for $\theta_{\pi q} \neq 0$, where σ_{LT} and σ_{TT} also contribute. Figure 9 shows simulated Q^2=6 GeV^2 SHMS+HMS data where θ_{SHMS} is varied $\pm 2^o$ from the 'near parallel' kinematic position. The excellent ϕ coverage allows σ_{LT} and σ_{TT} to be obtained in an efficient manner versus $-t$. The 5.50^o SHMS forward angle constraint limits some of the off-axis settings and causes some of the 'near parallel' settings to be offset slightly from the desired angle, as indicated in the right-most column of Table IV. The 'near parallel' offset is always $< 0.5^o$, which is substantially smaller than the maximum 1.3^o offset used in Fpi-2. At Q^2=0.3 GeV^2, the $-t$ acceptance is narrower, and so we propose to take an additional SHMS angle setting at $\theta_{\pi q} = +4^o$ to

TABLE IV: Proposed kinematics for the Fpi-12 experiment. The scattered electron will be detected in the HMS and the π^+ in the SHMS. The linac gradient key is: A: 2.15 GeV/pass "12.0"; B: 1.96 GeV/pass "10.9"; C: 1.82 GeV/pass "10.1"; D: 1.37 GeV/pass "7.6". The listed cross-section is for central-ray kinematics only, and should only be used as a rough guide.

E_e (Pass #)	$E_{e'}$	$\theta_{e'}$	ϵ	$\lvert t\rvert$	p_π	θ_π	$d^3\sigma/d^2\Omega dE$	SHMS $\theta_{\pi q}$
(GeV)	(GeV)	(deg)		(GeV^2)	(GeV)	(deg)	(pb/sr^{2}MeV)	Settings
Q^2=0.30 GeV^2, W=2.20 GeV								
2.80 (2D)	0.530	25.967	0.341	0.005	2.261	-5.710	20.06	0, $+2^o$,$+4^o$
3.70 (2C)	1.430	13.672	0.657	0.005	2.261	-8.326	98.16	0, $+2^o$,$+4^o$, -2^o
4.20 (3D)	1.930	11.037	0.747	0.005	2.261	-9.107	167.01	0, $+2^o$,$+4^o$, -2^o
Q^2=1.60 GeV^2, W=3.00 GeV								
6.60 (3A)	1.420	23.836	0.387	0.029	5.161	-6.183	5.51	0, $+2^o$
8.80 (4A)	3.620	12.866	0.689	0.029	5.161	-8.697	31.86	0, $+2^o$, -2^o
9.90 (5B)	4.720	10.616	0.765	0.029	5.161	-9.388	53.27	0, $+2^o$, -2^o
Q^2=2.45 GeV^2, W=3.20 GeV								
7.40 (4C)	1.107	31.734	0.265	0.048	6.265	-5.152	1.30	0.35^o, $+2^o$
8.80 (4A)	2.507	19.182	0.505	0.048	6.265	-7.298	5.62	0, $+2^o$, -1.8^o
9.90 (5B)	3.607	15.050	0.625	0.048	6.265	-8.305	11.15	0, $+2^o$, -2^o
10.90 (5A)	4.607	12.681	0.702	0.048	6.265	-8.972	17.81	0, $+2^o$, -2^o
Q^2=3.50 GeV^2, W=3.10 GeV								
7.90 (4B)	1.383	32.872	0.304	0.099	6.462	-6.358	0.76	0, $+2^o$
9.90 (5B)	3.383	18.602	0.587	0.099	6.462	-9.159	3.65	0, $+2^o$, -2^o
10.90 (5A)	4.383	15.555	0.671	0.099	6.462	-9.983	5.89	0, $+2^o$, -2^o
Q^2=4.50 GeV^2, W=3.28 GeV								
8.80 (4A)	1.138	39.155	0.220	0.122	7.594	-5.188	0.28	0.31^o, $+2^o$
9.90 (5B)	2.238	26.041	0.400	0.122	7.594	-7.101	0.83	0, $+2^o$, -1.60^o
10.90 (5A)	3.238	20.567	0.520	0.122	7.594	-8.227	1.56	0, $+2^o$, -2^o
Q^2=5.25 GeV^2, W=3.20 GeV								
8.80 (4A)	1.015	45.077	0.188	0.171	7.692	-5.081	0.16	0.42^o, $+2^o$
9.90 (5B)	2.115	28.997	0.373	0.171	7.692	-7.258	0.47	0, $+2^o$, -1.76^o
10.90 (5A)	3.115	22.677	0.498	0.171	7.692	-8.510	0.90	0, $+2^o$, -2^o
Q^2=6.00 GeV^2, W=3.20 GeV								
9.20 (5C)	1.015	47.244	0.177	0.212	8.070	-5.006	0.11	0.49^o, $+2^o$
9.90 (5B)	1.715	34.578	0.298	0.212	8.070	-6.543	0.23	0, $+2^o$, -1.04^o
10.90 (5A)	2.715	26.019	0.435	0.212	8.070	-8.014	0.50	0, $+2^o$, -2^o

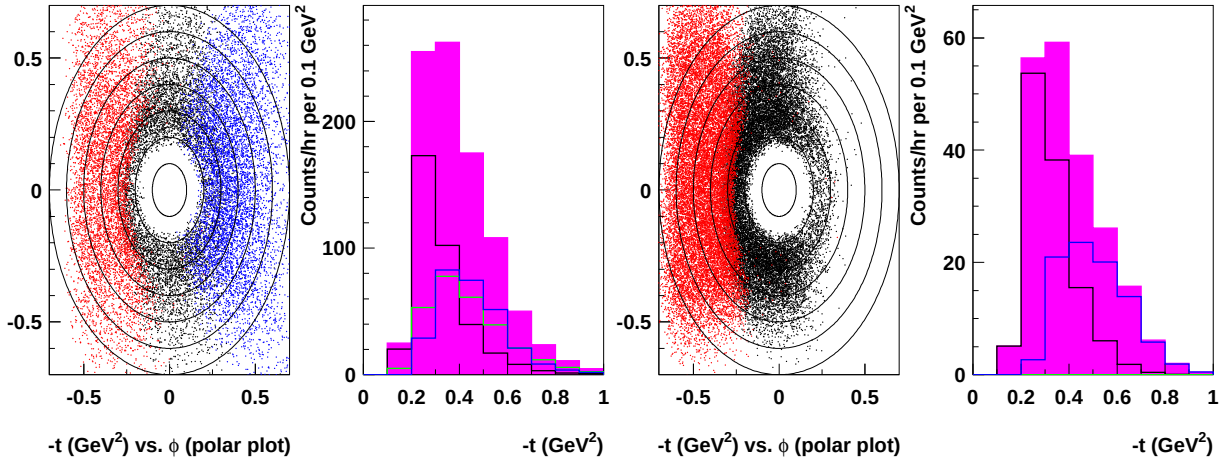

FIG. 9: Coverage of $-t$ (radial coordinate) versus azimuthal angle ϕ for the HMS+SHMS combination at $Q^2 = 6$ GeV^2. Cuts were placed to match the W-Q^2 range of the lowest ϵ setting. Each radial division corresponds to $-t = .10$ GeV^2. The left two plots are for the high ϵ runs at 10.90 GeV, with the SHMS set at 0 and $\pm 2.00^o$ degrees left and right of the nominal q-vector. The right two plots are for the two low ϵ runs at 9.20 GeV, with the SHMS set at 0.49^o and 2.00^o degrees right of the q-vector. The superposition of the three SHMS settings shows good ϕ coverage for the range $0.16 < |t| < 0.60$ GeV^2.

TABLE V: Anticipated HMS+SHMS detection efficiencies.

HMS tracking	0.95
SHMS tracking	0.95
pion absorption	0.95
pion decay (typical)	0.95
HMS: 5.9 msr acceptance for δ=-10% to +10%	0.9
SHMS: 3.5 msr acceptance for δ=-15% to +20%	0.9

extend the t-range for some values of ϕ.

VI. ANTICIPATED SINGLES RATES

All rate estimates assume the use of a 8 cm cryogenic target, and the detection efficiencies listed in Table V, unless otherwise noted.

A. Q^2=1.60-6.00 GeV^2 hydrogen data

Singles rates in the SHMS and HMS were examined for $p(e,e'\pi^+)$ data taking [33, 34], and are listed in the indicated columns of Table VI. The maximum beam current of 90 μA was assumed to be available. The projected singles rates are well below the anticipated capability of the detector packages, which we expect to be constructed with multi-MHz singles rates in mind. We note that at Q^2=6.0 GeV^2, the K^+ rate is as large as 70% of the π^+ rate. As the SHMS heavy gas Čerenkov is expected to achieve a better than $10^4:1$ π^+/K^+ rejection ratio at 8 GeV/c [35], this is not anticipated to be a problem. However, it does mean that care will have to be taken in the construction, operation, and calibration of this detector, to ensure that it meets its design goals.

For the purpose of calculating online random coincidence rates, the SHMS trigger rate was taken as equal to the raw trigger rate, i.e. no distinguishing between pions, kaons and protons in the SHMS trigger. Assuming an online π^- and K^- rejection rate of 25:1, the HMS trigger rate was taken to be electrons plus $(\pi^-+K^-)/25$. The random coincidence rate is then given by (SHMS trigger rate)(HMS trigger rate)Δt, where the coincidence resolving time was taken to be Δt=40 nsec. In all cases, the resulting online real + random rates are well below the expected capability of the HMS+SHMS data acquisition system. Offline, the relevant resolving time is expected to be no worse than 2 nsec and the reals to randoms ratio for electron-pion coincidences after missing mass cuts will only be a few percent for $p(e,e'\pi^+)n$.

B. Q^2=1.60-6.00 GeV^2 deuterium data

Because of lower currents (and hence longer beam times) required for the π^- measurements and the challenging experimental considerations outlined below, we will only measure the π^-/π^+ ratios at select values of Q^2=1.60 and 3.50 GeV^2.

Singles rates in the SHMS and HMS for deuterium target running are shown in the same Table VI. With the deuterium target, the positive polarity SHMS runs are expected to yield rates only about 10% higher than with the hydrogen target, and so are not recalculated in the table. The negative polarity SHMS runs have large projected e^- singles rates, and so the beam current for these runs has been reduced to 15 μA. With a judicious choice of kinematics, one is able to keep the SHMS electron rates in the vicinity of 1 MHz in the worst cases. In order to keep the random coincidence rate to acceptable levels, an electron veto trigger with efficiency $>$ 90% will almost certainly be necessary for the SHMS. An atmospheric Argon–Neon Čerenkov detector, perhaps in combination with the lead–glass calorimeter can be used to form this trigger. Random backgrounds after analysis cuts will be an order of magnitude larger for $d(e,e'\pi^\pm)$ than for $p(e,e'\pi^+)n$ because of the larger missing mass cut necessary.

TABLE VI: Projected SHMS and HMS rates from a 8 cm cryogenic target. LH+ indicates positive SHMS polarity running on a hydrogen target. LD- indicates negative SHMS polarity running on a deuterium target. The hadron rates vary relatively slowly with angle, so SHMS rates are shown only for the 'near parallel' setting. The electron rates are an extremely steep function of angle, and so SHMS electron rates are for the most forward angle of each setting. The HMS+SHMS random coincidence rates assume a resolving time of 40 ns and a 25:1 π^-, K^- rejection ratio, thus corresponding to the online rate only; offline cuts will reduce this number to a few percent of the reals.

	SHMS Singles Rates (kHz)						HMS Singles Rates (kHz)			Random coinc. (Hz)	Real coinc. (Hz)
	LH+ runs (90 μA)			LD- runs (15 μA)			LH+ runs (90 μA)			LH+ runs (90 μA)	
ϵ	π^+	K^+	p	e^-	π^-	K^-	e^-	π^-	K^-		
Q^2=1.60 GeV^2, W=3.00 GeV											
0.387	32	12	10	1130	4	0.1	6	54	22	20	3
0.689	26	10	10	200	4	0.3	54	24	2.0	100	32
0.765	24	10	8	90	4	0.3	110	200	1.8	210	64
Q^2=2.45 GeV^2, W=3.20 GeV											
0.265	14	8	5				1.0	38	1.2	2.8	0.5
0.505	14	7	5				8	19	1.2	9.2	5
0.625	12	5	4				20	14	1.2	17	10
0.702	10	4	4				40	8	0.8	29	20
Q^2=3.50 GeV^2, W=3.10 GeV											
0.266	10	5	4	900	2	0.3	0.8	12	0.6	1.0	0.4
0.563	4	2.0	1.8	200	1	0.1	8	4	0.4	2.6	3.7
0.652	3	1.6	1.4	80	0.6	0.1	14	2.6	0.4	3.8	7.3
Q^2=4.50 GeV^2, W=3.28 GeV											
0.220	6	4	2.4				0.4	12	0.4	0.4	0.1
0.400	4	2.4	1.8				1.4	5	0.4	0.5	0.6
0.520	3	1.6	1.2				3.4	3	0.2	0.8	1.5
Q^2=5.25 GeV^2, W=3.20 GeV											
0.188	6	3	2.2				0.2	8	0.2	0.2	0.06
0.373	3	1.8	1.4				0.8	3	0.2	0.2	0.4
0.498	1.6	1.0	0.8				2.0	1.6	0.2	0.3	0.9
Q^2=6.00 GeV^2, W=3.20 GeV											
0.177	3.6	2.6	1.8				0.2	6	0.2	0.2	0.05
0.298	2.8	2.0	1.4				0.2	3	0.2	0.1	0.2
0.435	1.4	1.0	0.8				0.5	1.2	0.2	0.1	0.5

Identification and tracking of π^- will also be complicated by the high electron singles rates in the SHMS. Assuming a ≈100 ns effective ADC gate for detectors that will be used to reject electrons, 1 MHz of electron singles implies that we will lose ≈1 MHz × 100 ns = 0.1 of the π^- sample. The large singles rates will also result in reduced tracking efficiency. This has been a key challenge in the analysis of π^- data from Fpi-2. Accurate determination of the tracking efficiency at high rates depends to a large extent on a very clean trigger; "junk hits" in trigger scintillators from soft photons complicates the efficiency determination greatly. The quartz hodoscope in the SHMS, however, should not be as sensitive to these issues, so will of much benefit in this case.

Measurement of the absolute electron beam current will also be a challenge for the π^- data set. The ≈150–200 nA noise in the baseline of the Unser current monitor (used to absolutely calibrate the resonating cavity beam current monitors) implies that we cannot verify that the current monitor calibration is stable to better than 1.3% at 15 μA. This potentially random uncertainty is unacceptable, so we plan to monitor the absolute luminosity via electron singles measured in the HMS. Since the HMS will be in exactly the same configuration for π^+ deuterium, running which will be taken at higher currents where the Unser noise is not a significant contribution to the normalization uncertainty, the electron singles for that data set can provide a direct calibration of the luminosity for the π^- data set.

C. Q^2=0.30 GeV^2 hydrogen data

Q^2=0.3 GeV^2 singles and accidental coincidence rates for $p(e, e'\pi^+)$ data taking are listed in Table VII. The Q^2=0.3 GeV^2 data require the SHMS to be at relatively low momentum and at forward angle. The projected π^+ singles rates are well within the anticipated capability of the SHMS detector package, but a potentially high accidental coincidence rate could result. To keep the random coincidence rate reasonably low would require us to reduce the beam current to 15 μA. This, however, would result in large point–to–point uncertainties in the beam current measurement. Hence, for the Q^2=0.3 GeV^2 data we assume a 4 cm target (as opposed to the 8 cm target assumed in the rest of the proposal) and a beam current of 30 μA. Because of this different target length and the fact that, as will be discussed later, we will need to remove the Argon–Neon gas Čerenkov from the SHMS for these data, this setting will likely require its own (very short) dedicated run period. Unfortunately, negative SHMS polarity running with these kinematics is expected to result in a nearly infinite rate of scattered electrons to the SHMS focal plane, and so will not be attempted.

TABLE VII: Projected SHMS and HMS rates from a 4 cm cryogenic target for the Q^2=0.3 GeV^2 setting. LH+ indicates positive SHMS polarity running on a hydrogen target. The hadron rates vary relatively slowly with angle, so SHMS rates are shown only for the 'near parallel' setting. The HMS+SHMS coincidence rates assume a resolving time of 40 ns and a 25:1 π^-, K^- rejection ratio, thus corresponding to the online rate only; offline cuts will reduce this number to a few percent of the reals.

	SHMS Singles Rates (kHz)			HMS Singles Rates (kHz)			Random coinc. (Hz)	Real coinc. (Hz)
	LH+ runs (30 μA)			LH+ runs (30 μA)			LH+ runs (30 μA)	
ϵ	π^+	K^+	p	e^-	π^-	K^-		
Q^2=0.30 GeV^2, W=2.20 GeV								
0.341	22	2	6	2	26	2	3.7	1.3
0.657	32	4	7	24	28	6	45	8.9
0.747	35	5	10	52	26	6	108	30

VII. KINEMATIC AND NORMALIZATION CHECKS WITH ELASTIC SCATTERING

The elastic ^{1}H$(e,e')p$ and ^{1}H$(e,e'p)$ reactions are extremely useful for systematic checks in single arm and coincidence spectrometer measurements. The fixed position of the elastic peak (W^2 in the single arm case, along with the missing energies and momenta in the two arm case) allow for relatively straightforward checks of the spectrometer central angles and momenta. The well-known elastic cross section provides easy verification of the knowledge of the product of the normalization and acceptance of the experiment.

Elastic scattering calibrations have been performed extensively in Hall C at lower energies and will play a significant role in the start–up and commissioning of the SHMS at 11 GeV. However, due to the strict systematic requirements of the F_π measurement, we will perform additional checks at kinematics as similar to those used in the F_π settings as possible. Below, we briefly the discuss the kinds of measurements we plan to make, as well as their relative feasibility and beam time requirements.

A. Single Arm Elastic Scans

Single arm elastic scans have been used extensively in Hall C to perform kinematic calibrations of both the HMS and SOS. While in principle, one is attempting to constrain three unknowns (beam energy, spectrometer central angle, and spectrometer central momentum) with one measurement (the hydrogen elastic peak), one can in fact use a body of data to provide very precise constraints.

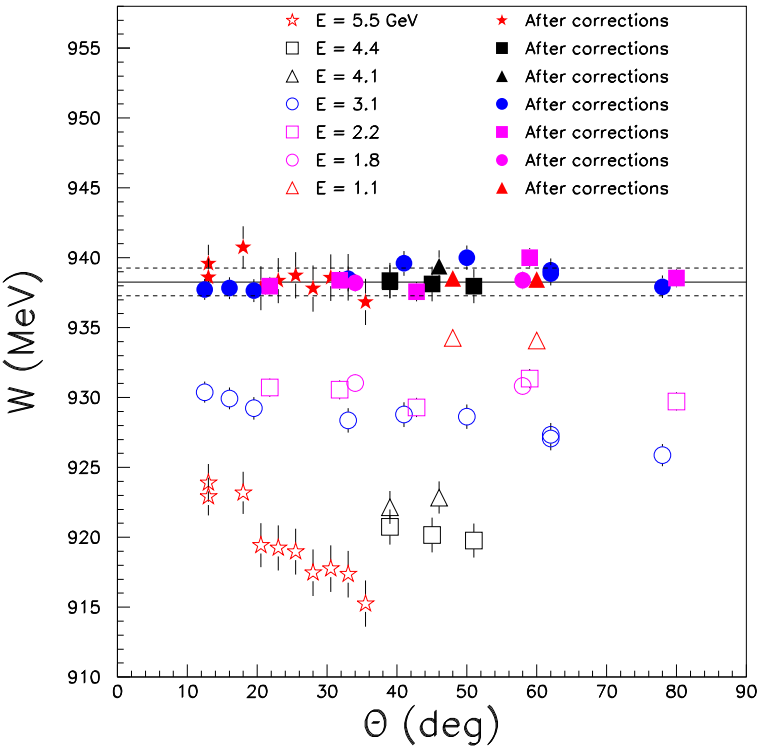

FIG. 10: ^{1}H$(e,e')p$ elastic peak offset as a function of central HMS angle for several beam energies. Open symbols are before fitting the HMS central momentum and angle offsets while the closed symbols show the deviations after fitting. A single angle and momentum offset was applied to the full data set. (Figure courtesy of Eric Christy, from Phys.Rev.C **70** (2004) 015206).

In the case of the HMS, we can rely on the fact that the rigid connection to the Hall C pivot ensures that variations in the spectrometer pointing will be relatively small as one rotates the spectrometer to various angles. Because of this excellent pointing, one can assume that, by and large, any offset to the spectrometer central angle is a fixed value, with minimal variation (on the order of 0.2 mrad) as the spectrometer is rotated. Similarly, one can assume that the deviation of the spectrometer central momentum is a fixed value due to the very linear response of the HMS dipole. Hence, by measuring the position of the reconstructed proton peak ($W = m_p$) over a range of angles and at several beam energies, one has several constraints on the spectrometer kinematic offsets. An example of such an analysis is shown in Fig. 10. In this analysis, the central scattering angle of the HMS was determined absolutely to 0.5 mrad while the point-to-point variation was estimated to be less than 0.2 mrad. The central HMS momentum was constrained to about 0.05%, with point-to-point variations on the order of 0.01-0.02%.

A similar such study of the SHMS is planned for the F_π experiment. In this case, the smaller angles and higher energies accessible give us a very large lever-arm for constraining

our knowledge of the central scattering angle and momentum. Fig. 11 shows the sensitivity of the elastic peak to the central spectrometer angle at 8.8 GeV. The elastic peak position shifts from $\sim$ -7 MeV/mrad to $\sim$ -17 MeV/mrad as one scans from 5.5 degrees to 18 degrees. At fixed beam energy, the dependence on the central spectrometer momentum is relatively flat, but by making measurements at several beam energies, one can deconvolute the angle and momentum offsets.

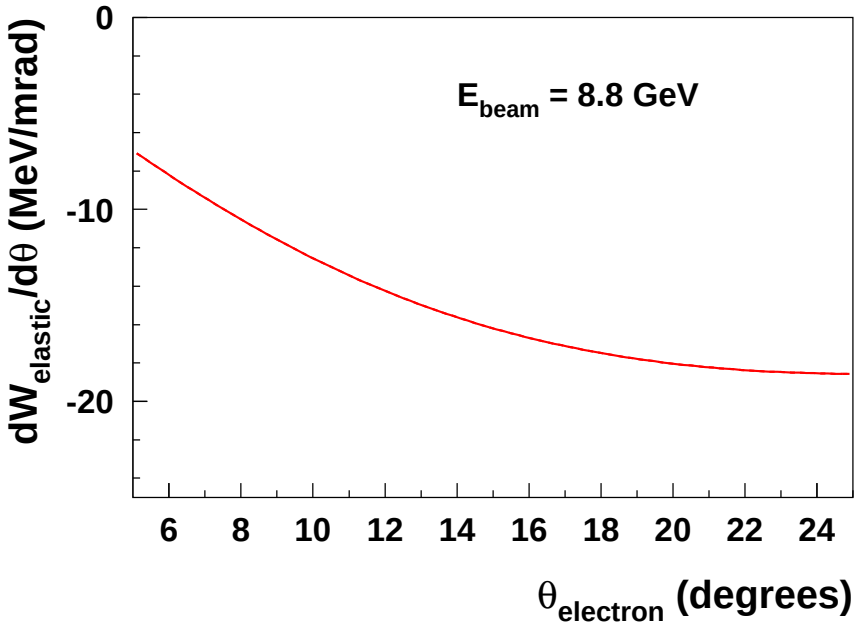

FIG. 11: Simulated ^{1}H$(e,e')p$ elastic peak offset as a function of scattered electron angle at a beam energy of 8.8 GeV. Over a relatively small range of angles (5.5 to 18 degrees) the shift in the elastic peak (per mrad central angle offset) varies by about 10 MeV.

A study of this nature can be carried out in parallel with data taking during the F_π experiment relatively easily. Rates are not a big issue, even at the largest energies. For the example in Fig. 11, one can acquire 10,000 elastic events in about 10 minutes at 18 degrees (assuming a 8 cm target and 90 μA). At a given beam energy, it should be straightforward to perform a useful SHMS angle scan in a few hours, including the overhead involved in changing the SHMS angle and momentum.

Given the success of such studies with the HMS, we feel we should be able to constrain the SHMS angle and momentum offsets with similar precision. The key to this method of course, is: 1) the rigid connection the Hall C pivot and good pointing reproducibility and 2) the linear response of the SHMS optics.

B. Coincidence Elastic Running

As noted above, one can amass a large body of (e, e') elastic data (for a single observable - the reconstructed proton mass) for a particular spectrometer to help constrain the momentum and angle offsets in that spectrometer. Alternatively, one can make use of the multiple observables available in the analogous coincidence reaction. In this case, one detects the scattered electron and recoiling proton in coincidence and reconstructs the proton mass (W^2), the missing energy (E_m), and the three components of the missing momentum ($P_m^{\perp}$,$P_m^{\parallel}$,P_m^{oop}).

In general, one prefers to take at least one coincidence elastic data point at each beam energy used by the experiment. It is also of benefit to choose the kinematics to sample a similar range of angle and momentum as used in the experiment. In Table VIII below, we list a few potential settings at higher beam energies. While one would like to use the elastic coincidence data to totally overlap the kinematics used in the experiment, this is not possible for all settings. Nonetheless, one can make measurements that access relatively small angles and high momenta for the SHMS, while accessing lower momenta and larger angles in the HMS. The only part of the experiment phase-space that is excluded is the smaller angle HMS settings, although undoubtedly single arm elastic scans can be used to fill in that missing area. The kinematics shown are of course not meant to represent a particular choice or plan, but to demonstrate that the SHMS+HMS combination has sufficient flexibility and range to sample the kinematics of interest.

TABLE VIII: Kinematics for potential ^{1}H$(e, e'p)$ calibration runs. For all but the first entry in the table below, the SHMS would be used as the electron arm, and the HMS as the proton arm. Rates listed assume 90 μA and a 8 cm LH_2 target.

E_{beam} (GeV)	Q^2 (GeV^2)	θ_e' (deg)	P_e' (GeV)	θ_p (deg)	P_p (deg)	Coincidence Rate (Hz)
*10.9	8.18	19.5	6.54	24.76	5.21	2.4
10.9	2.31	8.5	9.67	46.84	1.96	820
10.9	3.33	10.5	9.13	40.78	2.46	210
9.2	2.43	10.5	7.90	45.21	2.03	680
8.8	0.94	6.5	8.30	59.49	1.09	16000
7.4	0.49	5.5	7.14	66.88	0.74	92000
7.4	1.62	10.5	6.54	50.77	1.54	2800
7.4	2.79	14.5	5.91	41.49	2.24	400

* Protons detected in the SHMS.

C. Normalization Checks with Elastic Data

In addition to helping constrain the kinematic offsets as described above, all of the elastic data taken will enable us to check the normalization of the single arm and coincidence acceptance. In particular, examining the elastic yield across the spectrometer momentum acceptance has provided rigorous checks of our knowledge of the spectrometer response.

While most of the coincidence settings listed in Table VIII use the SHMS as the electron arm, it is useful to have at least one setting with the proton in the same spectrometer that will be used as the hadron arm in the F_π measurement (the SHMS). This allows us to: 1) verify that the central momentum offset does not change at positive polarity, 2) check for potential effects from hadrons (protons in this case) punching through the collimator and, 3) investigate hadron absorption effects in the detector stack. Runs with the SHMS at positive polarity are best done with the protons at relatively large momentum, hence must be taken at relatively large Q^2. The first entry in Table VIII indicates one such possible setting. In this case a run with ≈10,000 elastic events would take about 2 hours.

VIII. PARTICLE IDENTIFICATION

The SHMS will sit at very forward angles throughout the experiment. The detector package will be configured for π^+ or π^- detection, the two polarities presenting very different cases for particle identification. Above ~ 3 GeV/c pions cannot be reliably separated from protons via time of flight measurements over the 2.6 m baseline planned for the SHMS detector stack. The situation is of course even worse for pion and kaon separation. Good π^+/K^+ discrimination therefore requires a series of Čerenkov detectors. For the SHMS momenta that we require, this can be accomplished by a C_4F_{10} heavy gas Čerenkov, with momentum-dependent pressure from 0.7-2.0 atm (Fig. 12). The effect of the pressure change is to keep the optical characteristics of the Čerenkov approximately constant with momentum.

In the positive SHMS polarity case, the ratio of π^+/K^+ singles rates is of order 1. The kaons that propagate to the SHMS detector hut will be easily eliminated using the heavy gas Čerenkov. However, a significant fraction ($\approx 30\%$) of the kaons produced will decay to either charged muons or pions, some of which may propagate to the SHMS focal plane. These decay products will not be eliminated by the C_4F_{10} gas Čerenkov, however. Those resulting from kaon "singles" will show up as random coincidences and will be subtracted via the random coincidence subtraction. Decay products coming from real e^-K^+ coincidences cannot be eliminated in this manner. However, semi-inclusive and exclusive kaon production (along with its dominant decay products) has been simulated, and the contribution from these processes has been found to be $< 0.1\%$. The anticipated K^+ contamination due to real K^+ coincidences is shown in Fig. 13. We do not anticipate any difficulty caused by the projected

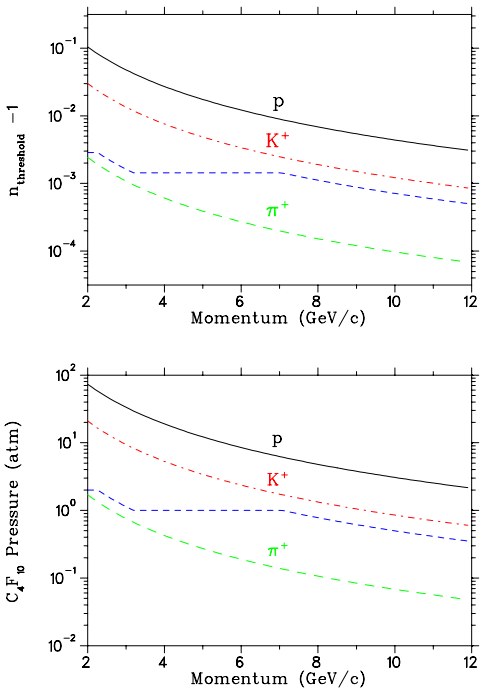

FIG. 12: Projected index of refraction and C_4F_{10} gas pressure versus SHMS momentum (dashed blue curve) necessary to ensure good $\pi^+ : K^+$ separation [35].

K^+ rates expected in this experiment.

When the SHMS is tuned for π^-, the e^-/π^- ratio is expected to sometimes be in excess of 1000:1, while the π^-/K^- ratio will be of order 10:1. An efficient gas Čerenkov detector, in combination with an electromagnetic calorimeter, will be required. An atmospheric Argon-Neon gas Čerenkov should yield at least 20:1 electron rejection, while the lead–glass calorimeter will provide 225:1 electron rejection. The total 4500:1 electron rejection should be adequate given the fact that the electron sample in the HMS will have virtually no contamination and therefore any remaining background in the SHMS should be (random) electron–electron coincidences. At this point, we should note that the Argon–Neon gas Čerenkov will be positioned in front of the SHMS drift chambers and could have detrimental effects on the resolution of reconstructed target quantities due to multiple scattering in the Čerenkov mirrors and windows. However, all the settings at which we will measure π^- electroproduction are at momenta of 5 GeV or above, so that resolution effects will be minimal. However, the Čerenkov will have to be removed for the Q^2=0.3 GeV^2 measurement. The Argon-Neon Čerenkov in combination with the calorimeter can also be used to form an electron veto at the trigger level.

Projected HMS rates in this experiment are low, and are expected to be well within the present operating parameters of HMS experiments. We plan to reject HMS π^- at the hardware level, identifying an electron by either a high preshower signal OR a high gas

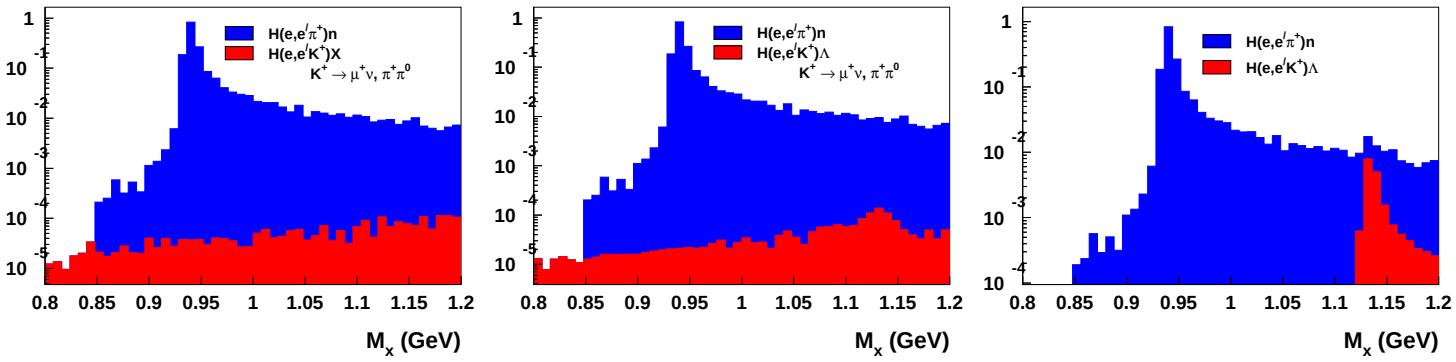

FIG. 13: Simulated K^+ contamination due to real electron-kaon coincidences between the HMS and SHMS for the Q^2=6.0 GeV^2 high ϵ setting (i.e. accidental coincidences have been eliminated via cuts). The first plot indicates the contribution due to semi-inclusive K^+ production, where the K^+ has decayed and the resulting μ^+ or π^+ have been detected in the SHMS. The second plot is similar, but for exclusive K^+ production. The final plot is also for exclusive K^+ production, but where the K^+ does not decay – in these kinematics the K^+ survival fraction in the SHMS is approximately 70%.

Čerenkov signal. In this case, the primary (non-prescaled) HMS trigger will be $S1 \bullet S2 \bullet$ *Electron*. π^- rejection rates of 25:1 should be possible without risking significant inefficiency. We will also allow a prescaled sample of pions to pass to monitor the trigger efficiency. After offline calorimeter, gas Čerenkov, coincidence time and missing mass cuts, the π^- contamination will be negligible, even in the worst case scenario.

While the primary event of interest will be HMS•SHMS, various prescaled HMS and SHMS singles events will also be taken in order to monitor the detector and trigger efficiencies and luminosity.

IX. NON-PHYSICS BACKGROUNDS

Once a combination of online hardware and offline software has determined that there was a coincidence between an electron in the HMS and a pion in the SHMS, there remain several backgrounds of the incoherent 'non-physics' variety: random coincidences and events from the target endcaps.

The electronic coincidence resolving window will be roughly 40 nsec. Offline, our excellent coincidence time resolution enables us to reduce the relevant resolving time to 2 nsec with negligible inefficiency. This is the first level of suppression of random coincidences. A cut

on the missing mass variable reduces the final random coincidence contamination to the few percent level. The missing (or undetected residual) mass is reconstructed from the final electron and detected hadron 4-momenta:

$$M_{res}^2 = P_{res}^2 = (P_e - P_{e'} + P_{tgt} - P_h)^2$$

The missing mass cut does a lot more than reduce random coincidences. To the extent that particle identification is flawless, real coincidences with larger inelasticity than $p(e, e'\pi^+)n$ (e.g. two pion electroproduction) are completely removed. The small contamination from the reaction $p(e, \pi^-\pi^+)p$, where the π^- is misidentified as an e^-, is heavily suppressed. Finally, model dependences of the experimentally determined cross sections due to radiative effects and decay muons are reduced as well.

Both spectrometers will view the aluminum target end windows in all configurations, so window background subtractions are necessary. Because the aluminum windows are each 4 mils thick, the ratio of protons in the windows to protons in the liquid hydrogen is about 10%. However, in Fpi-2, the surviving window background for $p(e, e'\pi^+)n$ after cuts was found to be only 1% [36]. The Hall C "empty" target consists of two 40 mil thick aluminum windows separated by 8 cm, which can tolerate up to 30 μA. Thus, our "empty" data come in 3 times = (40 mil $\times$ 30 μA) /(4 mil $\times$ 90 μA) faster than window events on the real target. Clearly our empty target measurement overhead will be small.

X. ANTICIPATED SYSTEMATIC UNCERTAINTIES

For most of the measurements proposed here, we have chosen the target length to be 8 cm. This is longer than the 4 cm typically used in L/T separation experiments in Hall C. In the past, we have been limited by the rather small y–target acceptance of the SOS. The SHMS y–target acceptance is quite large, and in any event the SHMS will sit at very small angles, so the extended target presents no problem. The HMS y–target acceptance could potentially be problematic since it will be used at rather large angles (up to $\approx$ 45 degrees). Fig. 14 shows both the delta and y–target acceptance of the HMS for an 8 cm target when the HMS sits at 50 degrees. Even for an 8 cm target, the HMS delta acceptance is quite flat. One can see that the extended target acceptance for the longer target is not totally flat, it does however, roll off rather slowly and smoothly. We anticipate minimal extra uncertainty due to the use of the longer target.

In comparison to the Fpi-2 experiment, which used the SOS for electron detection and the HMS for π^+ detection, we expect some improvements in the systematic uncertainty contributions.

- For electron detection, the HMS acceptance is much flatter than the SOS acceptance and will not suffer from magnetic field saturation. For pion detection, the SHMS is

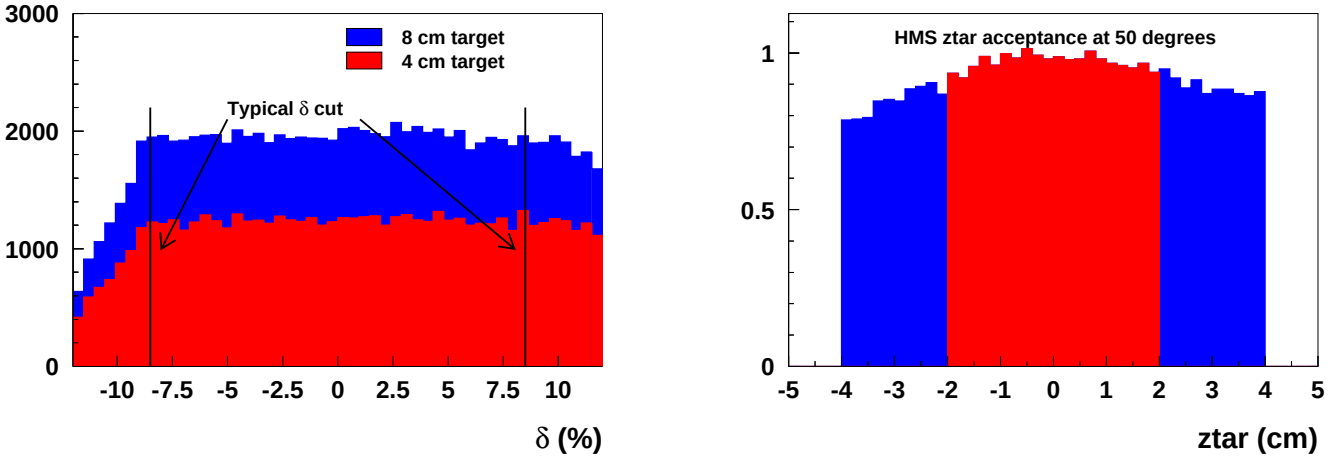

FIG. 14: Simulated momentum (δ) and z_{tar} distributions in the HMS spectrometer for 4 cm and 8 cm diameter targets and a HMS angle setting of 50^o. The δ distribution indicates no anomalies within the typically-accepted region. The z_{tar} distribution shows that events across the 8 cm target are contained within the HMS acceptance – the $\sim 10\%$ yield loss at the front and back edges is small and is expected to be easily understood.

expected to be comparable to the HMS in terms of its systematic error contribution. Therefore, the acceptance uncertainties have been reduced from our Fpi-2 experience.

- The higher π^+ momentum, in combination with the shorter SHMS flight-path, means that the pion decay correction will be less than half its value in the Fpi-2 experiment, and so its expected systematic uncertainty contribution has been scaled accordingly.

- The π^+ absorption correction is similarly expected to be smaller at higher pion momentum, and so has been reduced modestly from our Fpi-2 experience.

- We plan to acquire data at three ϵ settings, instead of the two used in Fpi-2. This is expected to result in somewhat smaller MC model uncertainties than in Fpi-2.

- Because of the presence of significant numbers of K^+, and the high e^- rates in the HMS, the particle identification (PID) will be somewhat more challenging than in Fpi-2. Thus, this systematic error has been doubled from our Fpi-2 uncertainty.

The resulting anticipated systematic uncertainties are listed in Table IX. Provided that extensive sieve-slit and other optics measurements are done during the first 12-18 months of SHMS operation, we expect these systematic uncertainties to be achievable, as they are based on our proven experience with the HMS+SOS.

TABLE IX: Anticipated systematic errors based on our Fpi-2 experience. The uncorrelated errors between the low and high ϵ settings are given in the first and second columns. The uncorrelated errors dominate the final error on F_π and have been conservatively estimated. The equivalent values determined in the Fpi-2 experiment are also listed, for comparison. The point-to-point uncertainties are magnified by $1/\Delta\epsilon$ in the L/T separation. The t-correlated uncertainties also suffer magnification. The scale uncertainties propagate directly into the separated cross sections.

	Type of systematic uncertainty		
	pt-to-pt	t-correlated	scale
Source	(%)	(%)	(%)
Acceptance	0.4	0.4	1.0
Target Thickness		0.2	0.8
Beam Charge		0.2	0.5
HMS+SHMS Tracking	0.1	0.1	1.5
Coincidence Blocking		0.2	
PID		0.4	
π Decay	0.03		0.5
π Absorption		0.1	1.5
Monte Carlo Generator	0.2	1.0	0.5
Radiative Corrections	0.1	0.4	2.0
Offsets	0.4	1.0	
Quadrature Sum	0.6	1.6	3.3
Fpi-2 Values	0.9	1.9	3.5

XI. PROJECTED ERROR BARS AND BEAM TIME ESTIMATE

To a good approximation in our kinematics, $\sigma_L \propto F_\pi^2$, so we need to first estimate the error on σ_L. Two measurements at fixed (Q^2, W) and different values of ϵ are needed in order to determine σ_L. Thus if $\sigma_1 = \sigma_T + \epsilon_1\sigma_L$ and $\sigma_2 = \sigma_T + \epsilon_2\sigma_L$ then

$$\sigma_L = \frac{1}{\epsilon_1 - \epsilon_2}(\sigma_1 - \sigma_2).$$

Assuming uncorrelated errors in the measurement of σ_1 and σ_2, we obtain the intermediate expression

$$\frac{\Delta\sigma_L}{\sigma_L} = \frac{1}{(\epsilon_1 - \epsilon_2)}\frac{1}{\sigma_L}\sqrt{\Delta\sigma_1^2 + \Delta\sigma_2^2}.$$

and by defining $r \equiv \sigma_T/\sigma_L$ and $\Delta\sigma/\sigma \equiv \Delta\sigma_i/\sigma_i$ and assuming $\Delta\sigma_1/\sigma_1 = \Delta\sigma_2/\sigma_2$, then

$$\frac{\Delta\sigma_L}{\sigma_L} = \frac{1}{\epsilon_1 - \epsilon_2}\frac{\Delta\sigma}{\sigma}\sqrt{(r+\epsilon_1)^2 + (r+\epsilon_2)^2}.$$

TABLE X: Projected errors for $F_\pi(Q^2)$ assuming the ϵ values given in Table IV, the projected uncertainties in Table IX, and 30,000 good coincidences per ϵ setting. An additional 1% model uncertainty in the form factor extraction is assumed.

Q^2 (GeV^2)	W (GeV)	$r \equiv \sigma_T/\sigma_L$	$\Delta\epsilon$	$\Delta F_\pi/F_\pi$ (%)
This Proposal				
0.30	2.20	0.63	0.41	5.2
1.60	3.00	0.18	0.38	3.6
2.45	3.20	0.19	0.44	3.0
3.50	3.20	0.32	0.37	4.0
4.50	3.28	0.38	0.30	4.3
5.25	3.20	0.56	0.31	5.0
6.00	3.20	0.73	0.26	6.6
Fpi-2 Final Errors				
1.60	2.21	0.48	0.27	4.9
2.45	2.21	0.80	0.28	6.0

This useful equation makes explicit the error amplification due to a limited ϵ range and (potentially) large r. For the proposed experiment, $r \leq 1$, so a limited ϵ lever arm is our primary source of uncorrelated error amplification, typically 3 here.

Again using the approximation that $\sigma_L \propto F_\pi^2$, the experimental error in F_π is

$$\frac{\Delta F_\pi}{F_\pi} = \frac{1}{2}\frac{1}{(\epsilon_1 - \epsilon_2)}\frac{\Delta\sigma}{\sigma}\sqrt{(r+\epsilon_1)^2 + (r+\epsilon_2)^2}.$$

As far as the extraction of the form factor is concerned, the relevant quantities are $r = \sigma_T/\sigma_L$ and $\Delta\epsilon$ between the two kinematic settings.

We assume that 30,000 good events per ϵ setting are used to determine the $-t$ dependence of the reaction (yet another small uncorrelated error). 30,000 events is the total per kinematic setting, but this is divided over 5 t-bins, giving us a statistical accuracy of 1.3%, to which is added the uncorrelated systematic error estimate in Table IX of 0.6%. This will allow the $-t$ dependence of σ_L to be carefully compared to the VGL Regge (or other) model. Note that the final uncertainty on F_π will be limited by the t-correlated uncertainty, which is common to all $-t$-bins at fixed ϵ, but varies randomly between ϵ settings. Since the final extraction of F_π will be dominated by the lowest $-t$ bin, the statistical precision of 1.3% per bin is well matched to the 1.6% t-correlated uncertainty.

The resulting projected error bars, including all statistical, systematic, and model fitting uncertainties, are listed in Table X and displayed in Fig. 15. We see that the proposed

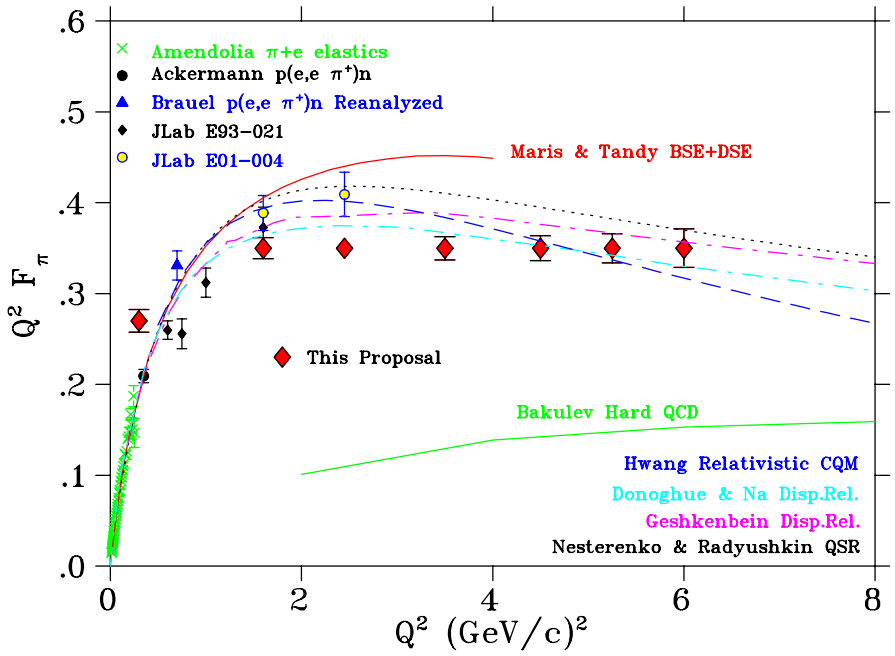

FIG. 15: Projected error bars for this SHMS+HMS proposal, in comparison with a variety of theoretical models, and existing precision data. The error bars include all projected statistical and systematic uncertainties, as well as an additional 1% model uncertainty in the form factor extraction added in quadrature.

measurement is easily able to distinguish between at least a number of the models.

We re-iterate the point that projected final uncertainties for F_π depend strongly on the ratio of transverse to longitudinal cross sections. For example, if $r = \sigma_T/\sigma_L$ were half the size, the uncertainty on F_π at $Q^2 = 6$ GeV^2 would shrink from 6.6% to about 4.5%. The T/L ratios assumed here in the calculation of our anticipated errors for the proposed measurements are listed in Table X. These assumed ratios are substantially more pessimistic than indicated by the VGL Regge model calculation (see Fig. 16), and so our error bar projection is realistically achievable by the experiment.

The uncertainty estimates described above have been tested using Monte Carlo data combined with an extraction of the pion form factor. One example is shown in Fig. 17. In the above formula, the statistical uncertainty is a bit overestimated since all t-bins will contribute to the extraction of F_π, so that the statistical precision is better than that assumed in a single bin. On the other hand, the contribution of the t-correlated systematic errors is a bit underestimated since these errors will affect the shape of the longitudinal cross section and impact the overall χ^2 of the fit. In the end, both these effects roughly cancel so that the simulated uncertainty is very close to the simple calculation (within 0.5%).

The estimated beam time in Table XI assumes 30,000 events per LH and LD(π^+) kine-

TABLE XI: Approximate running time for hydrogen and deuterium running. The number of hours per setting is for three $\theta_{\pi q}$ settings at high and medium ϵ and for two $\theta_{\pi q}$ settings at low ϵ (except at Q^2=0.3 GeV^2) as listed in Table IV. Times have been increased by 10% to account for additional time needed for data taking from the aluminum "dummy" target for cell wall substraction.

Q^2 (GeV^2)	ϵ	LH_2 Hours $p(e,e'\pi^+)n$	LD_2 Hours $d(e,e'\pi^+)nn$	LD_2 Hours $d(e,e'\pi^-)pp$	Overhead (Hours)	Total (Hours)
6.00	0.177	199	0	0	4	203
	0.298	106	0	0	4	110
	0.435	71	0	0	4	75
5.25	0.188	144	0	0	4	148
	0.401	52	0	0	4	56
	0.498	35	0	0	4	39
4.50	0.220	75	0	0	4	79
	0.400	30	0	0	4	34
	0.520	20	0	0	4	24
3.50	0.304	23	23	127	8	181
	0.587	8	0	0	4	12
	0.671	8	8	26	8	50
2.45	0.265	19	0	0	4	23
	0.505	8	0	0	4	12
	0.625	8	0	0	4	12
	0.702	8	0	0	4	12
1.60	0.387	8	8	13	8	37
	0.689	8	0	0	4	12
	0.765	8	8	8	8	32
0.30	0.341	8	0	0	4	12
	0.657	8	0	0	4	12
	0.747	8	0	0	4	12
Subtotals		862	47	174	104	
$p(e,e'p)$ + optics						80
9 beam energy changes						72

Grand Total: 1339 hours (56 days)

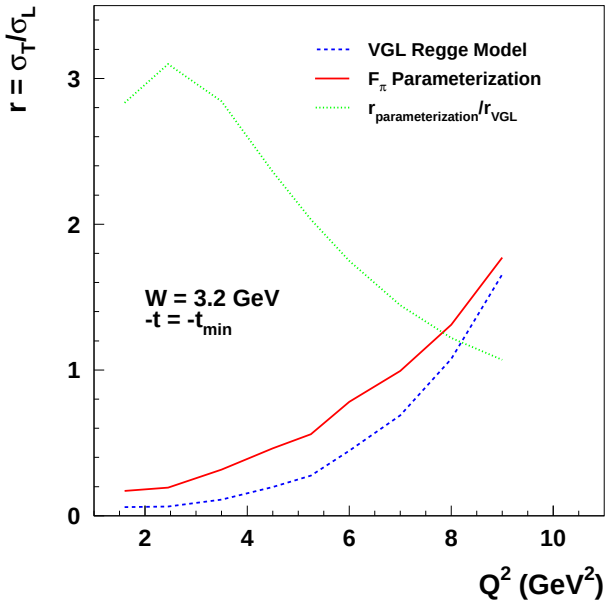

FIG. 16: Ratio of transverse to longitudinal cross sections, $r = \sigma_T/\sigma_L$ as calculated using the VGL Regge Model (blue dashed curve) and the parameterization used in this proposal (red solid curve). The green dotted curve denotes the super–ratio (our parameterization divided by VGL). The ratio r is calculated at $W = 3.2$ GeV and at $-t_{min}$. At low Q^2 and W, the VGL Regge model underpredicts the transverse cross section, however, one expects it to become increasingly accurate at larger W and Q^2. Nonetheless, our parameterization conservatively assumes that the Regge calculation still underpredicts the transverse cross section, even at $Q^2 = 6.0$ GeV^2.

matic setting, and 20,000 events per LD(π^-) setting, [1] including detection inefficiencies and cut inefficiencies. Times have been increased by 10% to account for data taking from the aluminum "dummy" target, needed to subtract contributions from the target cell walls. The beam current is assumed to be 90 μA for SHMS positive polarity runs, and 15 μA for SHMS negative polarity runs, incident on a 8 cm cryogenic target. Rates were estimated using SIMC, the Hall C Monte Carlo incorporating a parameterization of the ^{1}H$(e, e'\pi^+)$ cross section constrained by existing data at lower Q^2 but which asymptotically approaches VGL Regge predictions at larger Q^2. The overhead listed in the table will be used for target and momentum changes (extra time is allotted at points where we will take π^- data to allow time to change the SHMS polarity). We have also allocated $\approx$ one shift at each beam energy for elastic and optics data taking. An additional shift has been set aside for each beam energy change that will be required.

[1] Because of the neutron's smaller transverse cross section, the π^- data should have a L/T ratio at least two times larger than the π^+ data. The error amplification in the L/T separation will be smaller, hence, even with reduced statistics, the π^- longitudinal cross sections are expected to have uncertainties comparable to the π^+ data.

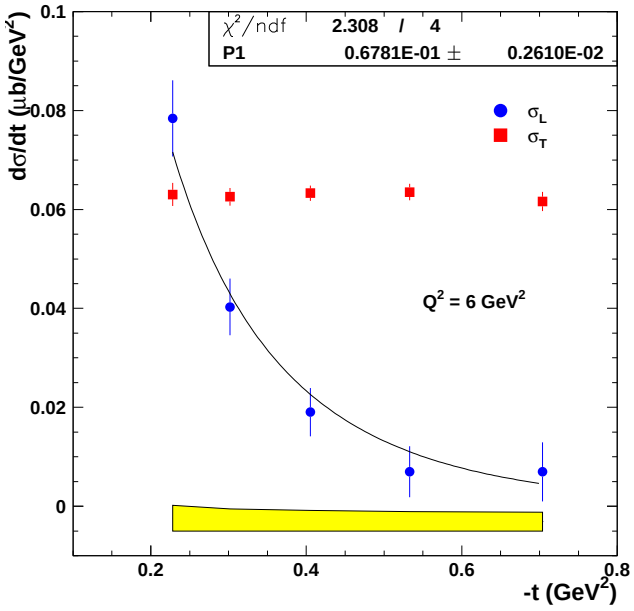

FIG. 17: Extraction of the pion form factor from simulated data at $Q^2 = 6$ GeV^2. A L–T separation was performed using simulated data from the three ϵ settings listed in Table IV and F_π was extracted by fitting the longitudinal cross section. The fit has one free parameter and the uncertainty shown on the plot reflects that coming from the statistical and point–to–point errors. There is an additional uncertainty coming from the t-correlated error (yellow band). The total uncertainty in F_π is very close to that estimated using the simple analytical expression discussed earlier (7.2% in this extraction, to be compared to 6.6%).

XII. HALL C AND SHMS DESIGN ISSUES

There are a number of issues which are relevant to the successful execution of this experiment and will be addressed during the detailed design phase of the upgraded Hall C. We enumerate here a few of the issues with which we are most concerned and we will appreciate the opportunity to provide input when the relevant design decisions are made.

SHMS detector hut shielding: One concern is the possibility that high energy particles, and in particular muons, could punch through the SHMS shielding hut when 11 GeV beam is used and the SHMS is at its most forward angle setting. This will have to be addressed, to ensure that the background from this source is limited to an acceptable level.

Beam pipe downstream of the target chamber: A concern which had significant implications during the running of Fpi-2 is the design of the downstream beampipe. In the Fpi-2 experiment, a rigid vacuum beampipe was used. To reach the minimum 10.5^o HMS angle, the beampipe must fit entirely inside a slot cut into the front face of HMS-Q1. In order to accommodate the Fpi-2 experiment, a narrow beampipe of special design was used. That narrow beam pipe mated directly to a much larger pipe via a thick flange. The thick flange in this transition region was a large source of background in the hall. If the beam tune

deviated from the nominal center by only the smallest of tolerances, the hall ion chambers recorded exceptionally high rates. The limiting of the allowed beam current when the HMS was $< 11.0^o$, in combination with the time lost to repeated beam tunes, both due to the sudden transition from narrow beampipe to very large beampipe, had a negative impact upon the experiment. In contrast, the narrow beampipe transition to large beampipe used during the Fpi-1 experiment caused none of these problems, even though it was filled with helium and was not under vacuum. In this case, the transition presented less material to the blown–up beam since a thick flange was not needed. This type of configuration might be an acceptable alternative. The extensive forward angle running required by this experiment necessitates that a more suitable solution to the downstream beampipe issue must be found, preferably while things are still in the design-stage.

Radiative heating of the SHMS bender magnet: The SHMS design incorporates a cryogenic bender magnet before the first quadrupole. The radiative heating of this bender needs to be evaluated in detail to make sure the SHMS can run at the high luminosities projected in this document.

XIII. SUMMARY

The high quality, continuous electron beam of Jefferson Lab makes it the only place to seriously pursue a program of F_π measurements. However, a challenge of the QCD-based models in the most rigorous manner requires the electron beam upgrade and construction of the SHMS.

The flexibility afforded by an 11 GeV maximum beam energy will allow measurements to be obtained sufficiently close to the π^+ pole that σ_L will be dominated by the t-channel process, and that backgrounds to σ_L will be minimized. The requirements upon the spectrometer are small forward angle capability, good angular reproducibility (to control systematic errors in the L/T separation) and sufficient missing mass resolution to cleanly separate $p(e,e'\pi^+)n$ events from $p(e,e'\pi^+)n\pi^0$. This combination will allow F_π to be determined in the best manner allowable by current models, and would provide a very significant advance in the understanding of the pion form factor.

Our proposed measurement of the pion form factor is a good match to the anticipated characteristics of the spectrometers and focal plane package and is a natural application of the proposed SHMS+HMS spectrometer system. Jefferson Lab can make a unique contribution to our knowledge of hadronic structure via this charged pion form factor experiment. We believe there is a strong case for this experiment to run within the first three years of the SHMS physics program.

XIV. ACKNOWLEDGEMENTS

The co-spokespersons would like to thank a number of people who have contributed to this proposal. Henk Blok and Dave Mack have provided many helpful comments and ideas over the years and contributed greatly to the final form of this proposal. Tanja Horn spent many hours and considerable effort perfecting the cross section parameterization used for all of the rate estimates, as well as providing a critical reading of the proposal. John Arrington and Pete Markowitz provided many helpful comments and ideas.

---

[1] G.R. Farrar, D.R. Jackson, Phys. Rev. Lett. **43** (1979) 246.
[2] N. Isgur, C.H. Llewellyn Smith, Phys. Rev. Lett. **52** (1984) 1080.
[3] O.C. Jacob, L.S. Kisslinger, Phys. Lett. **243B** (1990) 323.
[4] R. Jakob, P. Kroll, Phys. Lett. **315B** (1993) 463.
[5] C.R. Munz, et al., Phys. Rev. C **52** (1995) 2110.
[6] J.F Donoghue, E.S. Na, Phys. Rev. D **56** (1997) 7073.
[7] A.P. Bakulev, K. Passek-Kumericki, W. Schroers, N.G. Stefanis, Phys. Rev. D **70** (2004) 033014; and erratum **70** (04) 079906.
[8] B. Melic, B. Nizic, K. Passek, Phys. Rev. D **60** (1999) 074004.
[9] N.G. Stefanis, W. Schroers, H.-Ch. Kim, Eur. Phys. J. **C 18** (2000) 137.
[10] V.M. Braun, A. Khodjamirian, M. Maul, Phys. Rev. D **61** (2000) 073004.
[11] C.-W. Hwang, Phys. Rev. D **64** (2001) 034011.
[12] P. Maris, P.C. Tandy, Phys. Rev. C **62** (2000) 204.
[13] V.A. Nesterenko, A.V. Radyushkin, Phys. Lett. **115 B** (1982) 410.
[14] B.V. Geshkenbein, Phys. Rev. D **61** (2000) 033009.
[15] F.A. Berends, Phys. Rev. D **1** (1970) 2590.
[16] M. Vanderhaeghen, M. Guidal, J.-M. Laget, Phys. Rev. C **57** (1997) 1454.
M. Vanderhaeghen, M. Guidal, J.-M. Laget, Nucl. Phys. **A627** (1997) 645.
[17] W.R. Frazer, Phys. Rev. **115** (1959) 1763.
[18] B.H. Kellett, C. Verzegnassi, Nuo. Cim. **20A** (1974) 194.
[19] C.J. Bebek, et al., Phys. Rev. D **9** (1974) 1229.
[20] P. Brauel, et al., Z. Phys. C **3** (1979) 101.
[21] F. Gutbrod, G. Kramer, Nucl. Phys. **B49** (1972) 461.
[22] J. Volmer, et al., Phys. Rev. Lett. **86** (2001) 1713.
[23] V. Tadevosyan, et al., submitted to Phys. Rev. C, 2006.
[24] T. Horn, et al., submitted to Phys. Rev. Lett., 2006.
[25] H. Ackermann, et al., Nucl. Phys. **B137** (1978) 294.

[26] I. Obukhovsky, D. Fedorov, A. Faessler, Th. Gutsche, V.E. Lyubovitskij, Phys.Lett. **B 634** (2006) 220.
I. Obukhovsky, Private Communications, 2005-06.
[27] C.J. Bebek, et al., Phys. Rev. D **13** (1976) 25.
[28] C.J. Bebek, et al., Phys. Rev. Lett. **37** (1976) 1326.
[29] C.J. Bebek, et al., Phys. Rev. D **17** (1978) 1693.
[30] C.E. Carlson, J. Milana, Phys. Rev. Lett. **65** (1990) 1717.
[31] L. Mankiewicz, G. Piller, A. Radyushkin, Eur. Phys. J. **C 10** (1999) 307.
[32] S.R. Amendolia, et al., Phys. Lett. **146 B** (1984) 116.
S.R. Amendolia, et al., Nucl. Phys. **B 277** (1986) 168.
[33] wiser.f by Steve Rock. Wiser fit of $p^{\pm}$, $\pi^{\pm}$, $K^{\pm}$ cross sections $5< E <19$ GeV and $5< \theta <50^{o}$.
[34] rates.f by Eric Christy. Fit of electron elastic and inelastic scattering cross sections.
[35] Garth Huber, SHMS Heavy Gas Cerenkov Detector Design, April 1, 2002.
[36] Tanja Horn, Ph.D. Thesis, University of Maryland, 2006.